How does the Polar Dust affect the Correlation between Dust Covering Factor and Eddington Ratio in Type 1 Quasars Selected from the Sloan Digital Sky Survey Data Release 16?

Yoshiki Toba,[1,2,3] Yoshihiro Ueda,[1] Poshak Gandhi,[4] Claudio Ricci,[5,6] Denis Burgarella,[7] Veronique Buat,[7] Tohru Nagao,[3] Shinki Oyabu,[8] Hideo Matsuhara,[9,10] Bau-Ching Hsieh,[2]

[1] *Department of Astronomy, Kyoto University, Kitashirakawa-Oiwake-cho, Sakyo-ku, Kyoto 606-8502, Japan*

[2] *Academia Sinica Institute of Astronomy and Astrophysics, 11F of Astronomy-Mathematics Building, AS/NTU, No.1, Section 4, Roosevelt Road, Taipei 10617, Taiwan*

[3] *Research Center for Space and Cosmic Evolution, Ehime University, 2-5 Bunkyo-cho, Matsuyama, Ehime 790-8577, Japan*

[4] *Department of Physics and Astronomy, University of Southampton, Highfield, Southampton SO17 1BJ*

[5] *Núcleo de Astronomía de la Facultad de Ingeniería, Universidad Diego Portales, Av. Ejército Libertador 441, Santiago, Chile*

[6] *Kavli Institute for Astronomy and Astrophysics, Peking University, Beijing 100871, People's Republic of China*

[7] *Aix Marseille Univ. CNRS, CNES, LAM Marseille, France*

[8] *Institute of Liberal Arts and Sciences, Tokushima University, Minami Jousanjima-Machi 1-1, Tokushima, Tokushima 770-8502, Japan*

[9] *Institute of Space and Astronautical Science, Japan Aerospace Exploration Agency, 3-1-1 Yoshinodai, Chuo-ku, Sagamihara, Kanagawa 252-5210, Japan*

[10] *Department of Space and Astronautical Science, The Graduate University for Advanced Studies, SOKENDAI, 3-1-1 Yoshinodai, Chuo-ku, Sagamihara, Kanagawa 252-5210, Japan*

ABSTRACT

We revisit the dependence of covering factor (CF) of dust torus on physical properties of active galactic nuclei (AGNs) by taking into account an AGN polar dust emission. The CF is converted from a ratio of infrared (IR) luminosity contributed from AGN dust torus ($L_{\rm IR}^{\rm torus}$) and AGN bolometric luminosity ($L_{\rm bol}$), by assuming a non-linear relation between luminosity ratio and intrinsic CF. We select 37,181 type 1 quasars at $z < 0.7$ from the Sloan Digital Sky Survey Data Release 16 quasar catalog. Their $L_{\rm bol}$, black hole mass ($M_{\rm BH}$), and Eddington ratio ($\lambda_{\rm Edd}$) are derived by spectral fitting with `QSFit`. We conduct spectral energy distribution decomposition by using `X-CIGALE` with clumpy torus and polar dust model to estimate $L_{\rm IR}^{\rm torus}$ without being affected by the contribution of stellar and AGN polar dust to IR emission. For 5720 quasars whose physical quantities are securely determined, we perform a correlation analysis on CF and (i) $L_{\rm bol}$, (ii) $M_{\rm BH}$, and (iii) $\lambda_{\rm Edd}$. As a result, anti-correlations for CF–$L_{\rm bol}$, CF–$M_{\rm BH}$, and CF–$\lambda_{\rm Edd}$ are confirmed. We find that incorporating the AGN polar dust emission makes those anti-correlations stronger which are compared to those without considering it. This indicates that polar dust wind provably driven by AGN radiative pressure is one of the key components to regulate obscuring material of AGNs.

Keywords: Quasars (1319); Supermassive black holes (1663); Catalogs (205)

1. INTRODUCTION

An obscuring dusty structure surrounding a supermassive black hole (SMBH) plays an important role in the diversity of observational phenomena of active galactic nuclei (AGNs) in the context of unified model (e.g., Antonucci 1993; Urry & Padovani 1995). The obscuring material that is often called "dust torus" (e.g., Krolik & Begelman 1986) is expected to be compact (< 10 pc) and responsible for infrared (IR) emission from AGNs (e.g., Rees et al. 1969; Jaffe et al. 2004; Tristram et al. 2007).

Although it has been believed that dust torus is a key component of the AGNs, many challenges still remain; What is the structure of the circumnuclear dust? What is the main physical mechanism to regulate the obscuring material surrounding AGNs? These have been extensively studied both from theoretical side (e.g., Wada & Norman 2002; Schartmann et al. 2005; Fritz et al. 2006; Kawakatu & Wada 2008; Nenkova et al. 2008a,b;

Corresponding author: Yoshiki Toba

toba@kusastro.kyoto-u.ac.jp

Wada 2012, 2015; Siebenmorgen et al. 2015; Stalevski et al. 2016; Namekata & Umemura 2016; Tanimoto et al. 2019) and observational side (e.g., Suganuma et al. 2006; Ueda et al. 2007; Gandhi et al. 2009, 2015; Alonso-Herrero et al. 2011; Kishimoto et al. 2011; Ramos Almeida et al. 2011; Ricci et al. 2014; Brightman et al. 2015; Imanishi et al. 2016, 2018; Baba et al. 2018; Baloković et al. 2018; Izumi et al. 2018; Hönig 2019; Marchesi et al. 2019) (see also Netzer 2015; Ramos Almeida & Ricci 2017; Hickox & Alexander 2018, and references therein).

We focus here on the geometrical covering fraction of dust torus, a fundamental parameter in the AGN unified model. The dust covering factor (CF) is defined as the fraction of the sky, as seen from the AGN center, that is blocked by heavily obscuring dust. The CF also provides important information on the number of obscured AGNs. Many works have reported that the CF may depend on AGN luminosity wherein CF is often defined as type 2 AGN fraction (e.g., Simpson 2005; Toba et al. 2012, 2013, 2014, 2017), the IR-to-bolometric luminosity (e.g., Maiolino et al. 2007; Gandhi et al. 2009; Gu 2013; Ma & Wang 2013; Roseboom et al. 2013), or X-ray obscured AGN fraction (e.g., Ueda et al. 2003, 2014; Hasinger 2008; Burlon et al. 2011; Merloni et al. 2014) (but see also e.g., Dwelly & Page 2006; Lawrence & Elvis 2010; Mateos et al. 2017; Ichikawa et al. 2019 who reported weak or no significant dependence). The CF may also depend on redshift (e.g., La Franca et al. 2005; Hasinger 2008; Gu 2013; Merloni et al. 2014; Ueda et al. 2014) as well as counterargument of no significant evolution at least a certain redshift range (e.g., Toba et al. 2014; Vito et al. 2018).

Recently, Ricci et al. (2017) reported that the key parameter determining X-ray CF may be the Eddington ratio ($\lambda_{\rm Edd}$) rather than AGN luminosity (e.g., bolometric luminosity, $L_{\rm bol}$) based on 731 hard X-ray selected AGNs with a median redshift of 0.0367. Ezhikode et al. (2017) performed a correlation analysis for X-ray/optically selected 51 type 1 AGNs at $z < 0.4$, and combining the correlation analysis with simulations, they found that CF is more strongly anti-correlated with $\lambda_{\rm Edd}$ than with $L_{\rm bol}$. Zhuang et al. (2018) also reported that CF decreases with increasing $\lambda_{\rm Edd}$ up to ∼0.5 based on 76 Palomar-Green (PG) quasars at $z < 0.5$. Toba et al. (2019a) found that luminosity ratio of 6 μm and absorption-corrected hard X-ray luminosity for AGNs (that is expected to be an indicator of CF) depends on $\lambda_{\rm Edd}$, and that correlation would be applicable even for a Compton-thick AGN (Toba et al. 2020a).

On the other hand, Cao (2005) reported no correlation between the near-IR (NIR)-to-bolometric luminosity ratio (that is an indicator of CF) and $\lambda_{\rm Edd}$ for PG quasars, whereas there is a significant correlation between CF–$L_{\rm bol}$ and CF–the central black hole mass ($M_{\rm BH}$). These trends were also reported by Ma & Wang (2013) based on 17,639 quasars at $0.76 < z < 1.17$ selected from the Sloan Digital Sky Survey (SDSS: York et al. 2000).

The discrepancy in above works may be partially because the difference in sample selection, redshift distribution, and the definition of CF. In particular, statical works on CF for quasars tend to employ $L_{\rm IR}/L_{\rm bol}$ as CF. However, recent works suggested that $L_{\rm IR}/L_{\rm bol}$ may not be always a good indicator of CF caused by anisotropy in the IR emission of dust torus (e.g., Stalevski et al. 2016; Mateos et al. 2017; Zhuang et al. 2018). Because $L_{\rm IR}/L_{\rm bol}$ and CF are not connected by a simple linear relation, one needs a conversion from the luminosity ratio to the CF (see Section 3.3). In addition, the derived NIR luminosity for CF may be contaminated by stellar emission, which may not be negligible especially for less luminous quasars (e.g., Mateos et al. 2015; Toba et al. 2019a). Furthermore, more recently, polar dust wind probably driven by AGN radiative pressure has been shown to be an ubiquitous contributor to the IR emission (e.g., Hönig et al. 2013; Tristram et al. 2014; López-Gonzaga et al. 2016; Leftley et al. 2018; Asmus 2019; Stalevski et al. 2019). Lyu & Rieke (2018) demonstrated that the observed variety of their broad-band IR spectral energy distribution (SED) can be explained by considering polar dust component. As Asmus (2019) pointed out, we may need to take into account the polar dust emission when deriving CF from $L_{\rm IR}/L_{\rm bol}$.

In this work, we revisit the relationship between CF and $L_{\rm bol}$, $M_{\rm BH}$, and $\lambda_{\rm Edd}$ for type 1 quasars at $z < 0.7$ selected from the SDSS quasar catalog Data Release (DR) 16 (DR16Q; Lyke et al. 2020) that has been recently published. For this enormous number of type 1 quasars, we extract IR emission purely from dust torus after correcting for the stellar and polar dust emission based on the SED fitting with a clumpy torus model and polar dust model, and convert the luminosity ratio to intrinsic CF following Stalevski et al. (2016). This paper is organized as follows. Section 2 describes the sample selection of type 1 quasars, our SED modeling, and spectral fitting to the SDSS spectra. In Section 3, we present the results of the SED fitting, spectral fitting, and the dependence of CF on $L_{\rm bol}$, $M_{\rm BH}$, and $\lambda_{\rm Edd}$. In Section 4, we show a correlation analysis, and discuss possible uncertainties of the results and comparison of previous works. We summarize the results of the study in Section 5. Throughout this paper, the adopted cosmology is a flat universe with $H_0 = 70.0$ km s^{-1} Mpc^{-1},

$\Omega_M = 0.30$ and $\Omega_\Lambda = 0.70$. Unless otherwise noted, z refers to the spectroscopic redshift and an initial mass function (IMF) of Chabrier (2003) is assumed.

2. DATA AND ANALYSIS

2.1. Sample Selection

A flowchart of our sample selection process is shown in Figure 1. In this work, we focus on spectroscopically confirmed type 1 quasars whose $L_{\rm bol}$, $M_{\rm BH}$ and $\lambda_{\rm Edd}$ can be securely estimated. We sampled quasars that were drawn from the DR16Q (v4[1]) that contains 750,414 type 1 quasars up to $z \sim 6.0$.

Aside from the SDSS imaging data, 3.4 and 4.6 μm data taken from the Wide-field Infrared Survey Explorer (WISE; Wright et al. 2010) and information on source variability from the Palomar Transient Factory (PTF; Law et al. 2009; Rau et al. 2009) were used for target selection of quasars (see Sections 2.1 and 2.2 in Lyke et al. 2020, for more detail). The targeted objects were automatically classified as QSO, STAR, or GALAXY based on the SDSS spectra. In addition, objects that were initially classified as QSO at $z_{\rm pipe} > 3.5$ by the SDSS pipeline were reclassified for visual inspection (see Section 3.2 in Lyke et al. 2020).

Compared to previous SDSS quasar catalogs (e.g., DR7Q; Schneider et al. 2010, DR9Q; Pâris et al. 2012, and DR14Q; Pâris et al. 2018), DR16Q extends coverage of luminosity to much less luminous quasars given a redshift (see Figures 7 in Pâris et al. 2018 and Lyke et al. 2020). Hence our quasar sample is expected to cover a wide range of $L_{\rm bol}$, $M_{\rm BH}$, and $\lambda_{\rm Edd}$ compared with those derived from previous SDSS quasar catalogs employed in previous works on CF (e.g., Gu 2013; Ma & Wang 2013; Roseboom et al. 2013).

We first narrowed down the sample to objects with ZWARNING = 0, which ensures a confident spectroscopic classification and redshift measurement for quasars (Bolton et al. 2012). We then extracted objects with $0 < z < 0.7$ because we aim to estimate $M_{\rm BH}$ based on a recipe using Hβ (see Section 2.4) that is detectable for objects at z up to ~ 0.7 given a spectral coverage of SDSS spectrograph. Note that it is possible to measure $M_{\rm BH}$ for objects at $z > 0.7$ based on recipes using other emission lines (such as C IV and Mg II). But, to avoid being affected by possible systematic uncertainties of $M_{\rm BH}$ because of using different recipes, we adopted the same recipe for all quasars and perform a correlation analysis (see Sections 2.4 and 4.1). Eventually, 37,181 quasars were selected as a sample. We note that the number of
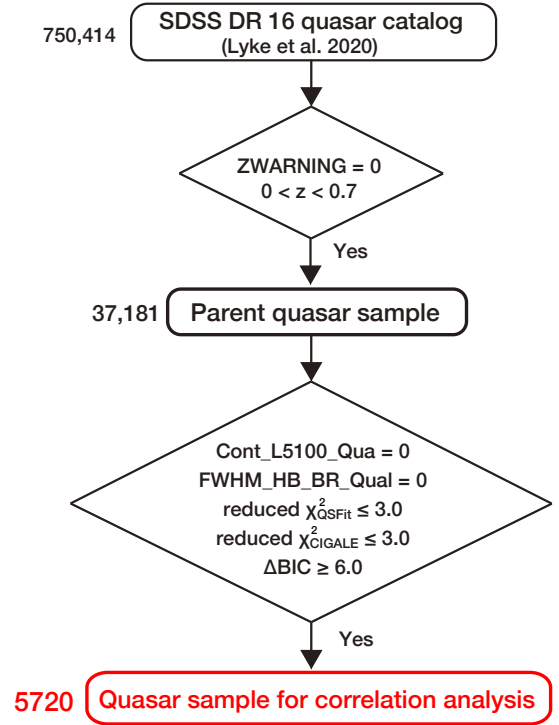
Figure 1. Flow chart of the process to quasar sample for a correlation analysis.

quasar sample at $z < 0.7$ selected from the DR16Q is significantly increased by $\sim$15,000 from DR14Q.

2.2. Photometric data

For those 37,181 quasars, we compiled optical to mid-IR (MIR) photometry, most of which are already available in DR16Q. In addition to SDSS optical data (u, g, r, i, and z) corrected for Galactic extinction (Schlafly & Finkbeiner 2011), we utilized the IR data taken with Two Micron All Sky Survey (2MASS; Skrutskie et al. 2006), the UKIRT Infrared Deep Sky Survey (UKIDSS; Lawrence et al. 2007), and the Wide-field Infrared Survey Explorer (WISE; Wright et al. 2010) (see Section 7 in Lyke et al. 2020 for a complete description of the above data).

Note that DR16Q newly employed unWISE (Lang 2014) instead of ALLWISE catalog (Cutri et al. 2014). unWISE provides deep 3.4 and 4.6 μm data that are force-photometered at the locations of SDSS sources (Lang et al. 2016). On the other hand, WISE 12 and 22 μm data are still quite useful for this work because those wavelengths are expected to trace the emission from the dusty torus (e.g., Toba et al. 2014). Hence we compiled those MIR data from ALLWISE with a search radius of $2''$ in the same manner as Pâris et al. (2018).

Consequently, we have at maximum 13 photometric data (u, g, r, i, z, Y, J, H, $K/K_{\rm s}$, and 3.4, 4.6, 12, and

22 μm) for the SED fitting (see Section 2.3). Among 37,181 quasars, 3345 (9.0 %), 5515 (14.8 %), 34,683 (93.3 %), and 37,155 (99.9 %) objects are detected by 2MASS, UKIDSS, ALLWISE, unWISE, respectively. We used profile-fit photometry for 2MASS-detected sources with rd_flg=2[2] and that for WISE 12 and/or 22 μm-detected sources with cc_flag=0[3] (which ensures clean photometry without being affected by possible artifacts) at each band. If an object lies outside the UKIDSS footprint, its NIR flux densities are taken from 2MASS (if that object is detected). Otherwise, we always refer to the UKIDSS as NIR data.

2.3. *Broad-band SED Fitting with* X-CIGALE

To derive IR luminosity contributed only from AGN dust torus ($L_{\rm IR}^{\rm torus}$), we conducted the SED fitting by considering the energy balance between the UV/optical and IR. We employed a new version of Code Investigating GALaxy Emission (CIGALE; Burgarella et al. 2005; Noll et al. 2009; Boquien et al. 2019) so-called X-CIGALE[4] (Yang et al. 2020). This code enables us to handle many parameters, such as star formation history (SFH), single stellar population (SSP), attenuation law, AGN emission, dust emission, and radio synchrotron emission (see e.g., Boquien et al. 2014; Buat et al. 2014, 2015; Boquien et al. 2016; Ciesla et al. 2017; Lo Faro et al. 2017; Toba et al. 2019b; Burgarella et al. 2020). Aside from an implementation of the SED fitting even for X-ray data, X-CIGALE incorporates a clumpy two-phase torus model (SKIRTOR[5]; Stalevski et al. 2012, 2016) and a polar dust emission as AGN templates. According to Yang et al. (2020), we consider the dust responsible for type 1 AGN obscuration as polar dust (i.e.., the polar dust provides obscuration for the nucleus and the additional IR emission from the absorbed energy, see Figure 4 in Yang et al. 2020 for a schematic view of polar dust). Parameter ranges used in the SED fitting are tabulated in Table 1.

We adopted a delayed SFH model, assuming a single starburst with an exponential decay (e.g., Ciesla et al. 2015, 2016), where we fixed the age of the main stellar population in the galaxy that is the same as what we used for galaxy template when fitting to the SDSS spectra (see Section 2.4). We parameterized e-folding time of the main stellar population ($\tau_{\rm main}$). The influence of

[2] https://old.ipac.caltech.edu/2mass/releases/allsky/doc/sec4_4d.html
[3] http://wise2.ipac.caltech.edu/docs/release/allsky/expsup/sec4_4g.html
[4] https://gitlab.lam.fr/gyang/cigale/tree/xray
[5] https://sites.google.com/site/skirtorus

Table 1. Parameter Ranges Used in the SED Fitting with X-CIGALE

Parameter	Value
Delayed SFH	
$\tau_{\rm main}$ (Gyr)	0.5, 1.0, 2.0, 4.0, 6.0, 8.0
age (Gyr)	5.0
SSP (Bruzual & Charlot 2003)	
IMF	Chabrier (2003)
Metallicity	0.02
Dust Attenuation (Charlot & Fall 2000)	
$A_{\rm V}^{\rm ISM}$	0.01, 0.1, 0.2, 0.3, 0.4, 0.6, 0.8, 1.0
slope_ISM	-0.7
slope_BC	-1.3
AGN Disk +Torus Emission (Stalevski et al. 2016)	
$\tau_{9.7}$	3, 5, 9
p	0.0, 1.0, 1.5
q	0.0, 1.0, 1.5
Δ ($^\circ$)	10, 30, 50
$R_{\rm max}/R_{\rm min}$	30
θ ($^\circ$)	0
$f_{\rm AGN}$	0.5, 0.6, 0.7, 0.8, 0.9, 0.99
AGN Polar Dust Emission (Yang et al. 2020)	
extinction low	SMC
$E(B-V)$	0.0, 0.05, 0.1, 0.15, 0.2, 0.3, 0.4
$T_{\rm dust}^{\rm polar}$ (K)	100.0, 500.0, 1000.0
Emissivity β	1.6

fixing the age of the main stellar population on CF is discussed in Section 4.3.

We chose the SSP model (Bruzual & Charlot 2003), assuming the IMF of Chabrier (2003), and the standard nebular emission model included in X-CIGALE (see Inoue 2011).

For attenuation of dust associated with host galaxy, we utilized a model provided by Charlot & Fall (2000) that has two different power-law attenuation curves; the power law slope of the attenuation in the interstellar medium (ISM) and birth clouds (BC) that were fixed in this work. We parameterized the V-band attenuation in the ISM ($A_{\rm V}^{\rm ISM}$).

AGN emission from accretion disk and dust torus was modeled by using the SKIRTOR, a clumpy two-phase torus model produced in the framework of the 3D radiative-transfer code, SKIRT (Baes et al. 2011; Camps & Baes 2015). This torus model consists of 7 parameters; torus optical depth at 9.7 μm ($\tau_{9.7}$), torus density radial parameter (p), torus density angular parameter (q), angle between the equatorial plane and edge of the torus (Δ), ratio of the maximum to minimum radii of the torus ($R_{\rm max}/R_{\rm min}$), the viewing angle (θ), and the

AGN fraction in total IR luminosity ($f_{\rm AGN}$). In order to avoid a degeneracy of AGN templates (see Yang et al. 2020) and to estimate a reliable CF (see Section 3.3), we fixed $R_{\rm max}/R_{\rm min}$ and θ that are optimized for type 1 quasars. We note that $R_{\rm max}/R_{\rm min}$ and θ are insensitive to the CF at least for type 1 AGNs as Stalevski et al. (2012) reported.

In X-CIGALE, the polar dust emission is implemented as a gray body emission with an empirical extinction curve (see Section 2.4 in Yang et al. 2020, for more detail). The gray body is formulated as $1 - e^{\tau(\nu)}$ $\nu^{\beta} B_{\nu}(T_{\rm dust}^{\rm polar})$, where ν is the frequency, β is the emissivity index of the dust, and $B_{\nu}(T_{\rm dust}^{\rm polar})$ is the Planck function. $\tau \equiv (\nu/\nu_0)^{\beta}$ is the optical depth. ν_0 is the frequency where optical depth equals unity (Draine 2006). $\nu_0 = 1.5$ THz ($\lambda_0 = 200\ \mu$m) in X-CIGALE and β is fixed to be 1.6 (e.g., Casey 2012), and thus we parameterized $T_{\rm dust}^{\rm polar}$ in the same manner as Toba et al. (2020b). We adopted the SMC extinction curve (Prevot et al. 1984) that may be reasonable for AGN dust (e.g., Pitman et al. 2000; Kuhn et al. 2001; Salvato et al. 2009), in which we parameterized $E(B-V)$. $E(B-V) = 0$ means that polar dust component is not necessary. We confirmed that our conclusion is not significantly affected if we assumed another extinction curve.

In the framework of our SED modeling, IR luminosity can be described by a combination of stellar component ($L_{\rm IR}^{\rm stellar}$), AGN accretion disk component ($L_{\rm IR}^{\rm disk}$), AGN dust torus component ($L_{\rm IR}^{\rm torus}$), and AGN polar dust component ($L_{\rm IR}^{\rm polar}$), which enables to estimate $L_{\rm IR}^{\rm torus}$ that is relevant to CF through the SED decomposition.

Under the parameter setting described in Table 1, we fit the stellar and AGN (accretion disk, dust torus, and polar dust) components to at most 13 photometric data as described in Section 2.2. Although the photometry employed in DR16Q is not identical, the profile-fit photometry is used for the SDSS and 2MASS (Lyke et al. 2020), while the UKIDSS and unWISE data are forced-photometry at the SDSS centroids (Aihara et al. 2011; Lang 2014). Therefore, the flux densities in the optical-MIR bands in DR16Q are expected to trace the total flux densities, suggesting that the influence of different photometry is likely to be small (see also Section 4.5). We used flux density in a band when the signal-to-noise ratio (S/N) is greater than 3 at that band. Following Toba et al. (2019a), we put 3σ upper limits for objects with ph_qual='U' (which means upper limit on magnitude) in the MIR-bands.

2.4. *Optical Spectral Fitting with* QSFit

In order to derive $M_{\rm BH}$, $L_{\rm bol}$, and $\lambda_{\rm Edd}$ of our quasar sample, we conducted a spectral fitting to SDSS spectra

by using the Quasar Spectral Fitting package (QSFit v1.3.0; Calderone et al. 2017)[6]. This code fits optical spectra by taking into account (i) AGN continuum with a single power law, (ii) Balmer continuum modeled by Grandi (1982) and Dietrich et al. (2002), (iii) host galaxy component with an empirical SED template, (iv) iron blended emission lines with UV-optical templates (Véron-Cetty et al. 2004; Vestergaard & Wilkes 2001), and (v) emissions line with Gaussian components. QSFit fits all the components simultaneously following a Levenberg-Marquardt least-squares minimization algorithm with MPFIT (Markwardt 2009) procedure.

The main purpose of this spectral fitting is to measure FWHM of Hβ broad component ($FWHM_{\rm H\beta}$) and continuum luminosity at 5100Å (L_{5100}) that are ingredients for $M_{\rm BH}$ estimates. For the host galaxy contribution[7], we employed a simulated 5 Gyr old elliptical galaxy template (Silva et al. 1998; Polletta et al. 2007) with allowing the normalization to vary. After correcting the Galactic extinction provided by Schlafly & Finkbeiner (2011) that is same as what we adopted for the SDSS photometry (see Section 2.2), spectral fitting was executed. Following Calderone et al. (2017), we fit the Hβ line with narrow and broad components in which the FWHM of narrow and broad components is constrained in the range of 100 to 1000 and 900 to 15,000 km s^{-1}, respectively to allow a good decomposition of the line profile.

Based on outputs from QSFit, we estimated $M_{\rm BH}$ with a single-epoch method reported by Vestergaard & Peterson (2006);

$$\log\left(\frac{M_{\rm BH}}{M_{\odot}}\right) = \log\left[\left(\frac{FWHM_{\rm H\beta}}{1000\,{\rm km\,s^{-1}}}\right)^2 \left(\frac{L_{5100}}{10^{44}\,{\rm erg\,s^{-1}}}\right)^{0.50}\right]$$
$$+ (6.91 \pm 0.02). \qquad (1)$$

$L_{\rm bol}$ was converted from $BC_{5100} \times L_{5100}$ where BC_{5100} = 8.1 ± 0.4 is the bolometric correction (Runnoe et al. 2012). The uncertainty in $M_{\rm BH}$ is calculated through error propagation of Equation 1 while the uncertainty in $L_{\rm bol}$ is propagated from 1σ errors of L_{5100} and BC_{5100}.

3. RESULTS

Here we present physical properties of 37,181 quasars that are derived from the SED fitting with X-CIGALE and spectral fitting with QSFit, which are summarized in Table 2.

---

[6] https://qsfit.inaf.it

[7] Since QSFit allows to fit the host galaxy component for objects at $z < 0.8$ by default (see Section 2.4 in Calderone et al. 2017), our spectral fitting to the quasar sample (at $z < 0.7$) always takes into account the contribution of host galaxy to the continuum.
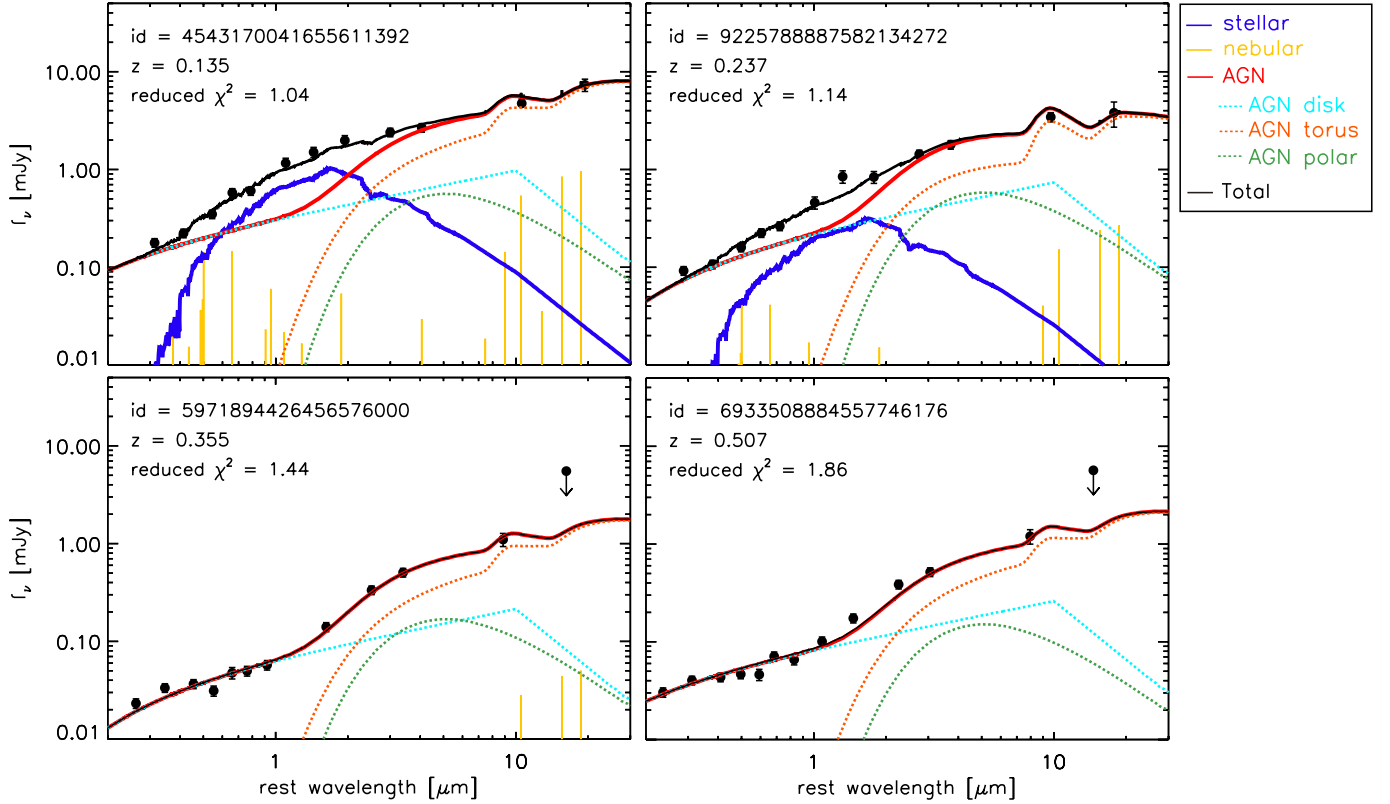
Figure 2. Examples of the SED fitting with `X-CIGALE`. The black points are photometric data. The contribution from the stellar, nebular, and AGN components to the total SED are shown as solid blue, yellow, and red lines, respectively. The contribution from AGN accretion disk, dust torus, and polar dust components to the total AGN emission are plotted as dashed cyan, orange, and green lines, respectively. The black solid lines represent the resultant best-fit SED.

3.1. *Result of the SED Fitting and Bayesian Information Criterion*

Figure 2 shows examples of the SED fitting with `X-CIGALE`. We confirm that $34{,}541/37{,}181$ (~ 92.9 %) objects have reduced $\chi^2_{\rm CIGALE} < 3.0$, meaning that the data are well fitted with the combination of the stellar, nebular, AGN accretion disk, dust torus, and polar dust components by `X-CIGALE`.

On the other hand, it is worth investigating whether polar dust component (that is the main topic in this work) is practically needed to improve the SED fitting. In order to test the requirement to add an AGN polar dust component to the SED fitting, we calculate the Bayesian information criterion (BIC; Schwarz 1978) for two fits that are derived with and without polar dust component. The BIC is defined as BIC = $\chi^2 + k \times \ln(n)$, where χ^2 is non-reduced chi-square, k is the number of degrees of freedom (DOF), and n is the number of photometric data points used for the fitting. We then compare the results of two SED fittings without/with polar dust component by using ΔBIC = BIC$_{\rm wopolar}$ − BIC$_{\rm wpolar}$. The resultant ΔBIC tells whether or not the AGN polar dust component is required to give a better
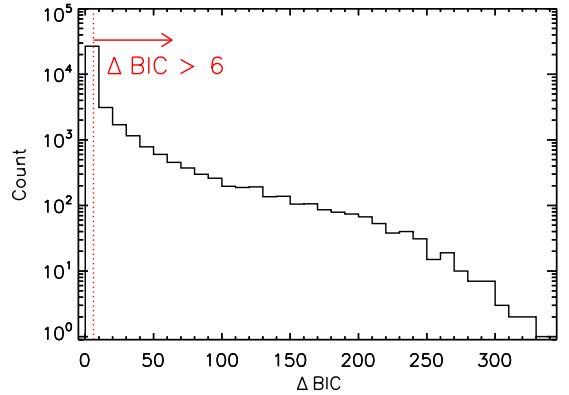
Figure 3. Histogram of ΔBIC = BIC$_{\rm wopolar}$–BIC$_{\rm wpolar}$ for the quasar sample. The red dotted line corresponds to ΔBIC = 6 that is a threshold to consider the differences in two fits with and without adding polar dust component.

fit with taking into account the difference in DOF (e.g., Ciesla et al. 2018; Buat et al. 2019; Aufort et al. 2020; Toba et al. 2020c). Figure 3 shows the histogram of ΔBIC for our quasar sample. We adopt ΔBIC = 6 as a threshold to consider the differences in two fits in the same manner as Buat et al. (2019). If ΔBIC > 6, this indicates that adding the AGN polar dust compo-
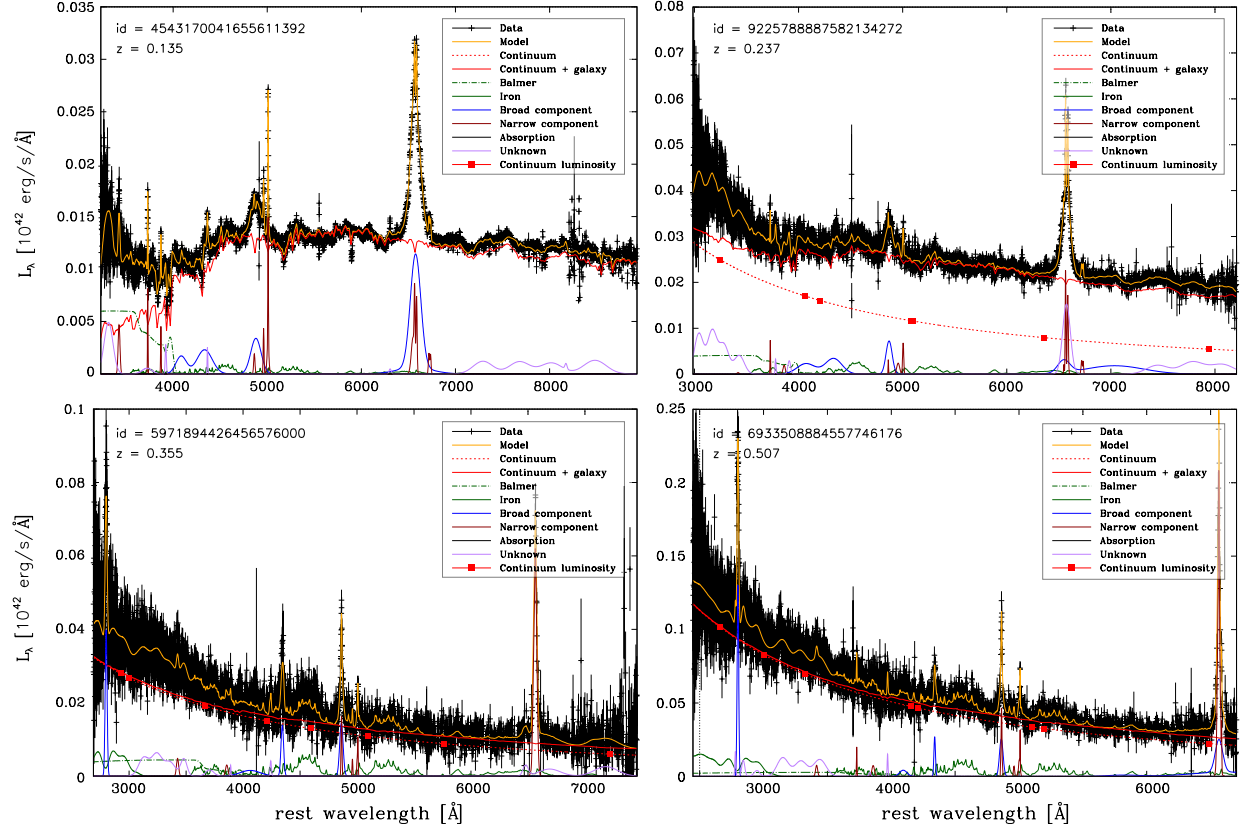
Figure 4. Examples of optical spectral fitting with `QSFit`. The same objects plotted in Figure 2 are presented. The black crosses are observed data. The power-law continuum is shown in dotted red lines while the power-law continuum plus AGN host components are shown in solid red lines. The green dash-dotted and solid curves denote the Balmer continuum and iron continuum, respectively. The brown and blue solid curves show the narrow and broad components of emission lines, respectively. The best-fit spectrum is shown in yellow lines.

nent significantly improves the fit. We find that about 30.0% of objects satisfy ΔBIC > 6. This suggests that for a faction of objects in our SDSS quasar sample at $z < 0.7$, an AGN polar dust component may not be necessary. We note that the threshold we adopted in this work is conservative compared to what originally suggested to be ΔBIC $= 2$ (Liddle 2004; Stanley et al. 2015). Nevertheless, the above result could suggest that our SED modeling may not be enough to constrain of the AGN polar dust emission given a limited number of photometric data in MIR regime, which we should keep in mind for the following analysis. We remind that the main purpose of this work is to see how the AGN polar dust would affect the CF of type 1 quasars. Hence, we consider objects with $\chi^2_{\mathrm{CIGALE}} < 3.0$ and ΔBIC > 6 for the correlation analysis (see Section 3.3).

3.2. *Result of the Spectral Fitting*

Figure 4 shows examples of the optical spectral fitting with `QSFit`. We confirm that 36,855/37,181 ($\sim$99.1%) objects have reduced $\chi^2_{\mathrm{QSFit}} < 3.0$ while only 170 ($\sim$0.5 %) objects are failed to fit due to low S/N. This indicates

that the SDSS spectra of our sample are well-fitted by `QSFit`. Note that objects showing top panel in Figure 4 are expected to have large contribution from host galaxy to optical spectrum according to the SED fitting (see top panel in Figure 2). We confirm this is the case for their optical spectra, suggesting that our SED modeling and spectral fitting give consistent results.

In addition to goodness of fitting (i.e., χ^2_{QSFit}), `QSFit` provides "quality flags" for measurements to assess the reliability of the results (see Appendix C in Calderone et al. 2017, for more detail). We considered `Cont_5100_Qual` and `HB_BR_Qual` that are relevant to the reliability of M_{BH} and L_{bol} (see also Table 2). We find that L_{5100} and $FWHM_{\mathrm{H}\beta}$ are securely estimated for 21,888/37,181 ($\sim$58.9%) objects. To ensure the accuracy of fitting results, we focus objects with $\chi^2_{\mathrm{QSFit}} < 3.0$, `Cont_5100_Qual` $= 0$, and `HB_BR_Qual` $= 0$ for the following analysis (see Section 3.3).

The distributions of our sample with `Cont_5100_Qual` $= 0$ and `HB_BR_Qual` $= 0$ in $z - L_{\mathrm{bol}}$ and $M_{\mathrm{BH}} - L_{\mathrm{bol}}$ plane are shown in Figures 5 and 6, respectively. The mean and standard deviation of $\log L_{\mathrm{bol}}$ (erg s^{-1}),
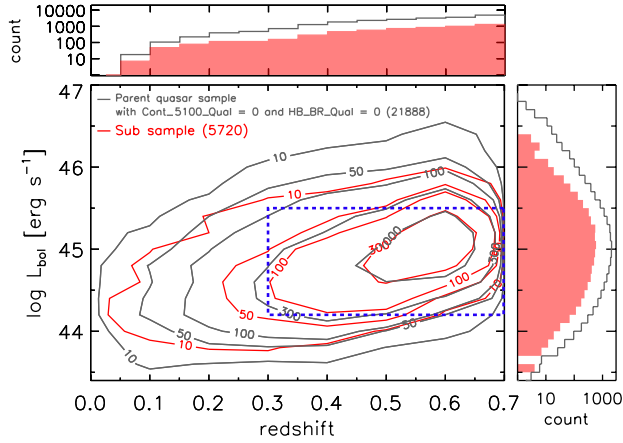
Figure 5. The bolometric luminosity as a function of redshift for our sample. The histograms of redshift and $L_{\rm bol}$ are attached on the top and right, respectively. The gray and red contours represent the number density of 21,888 objects with `Cont_5100_Qual` = 0 and `HB_BR_Qual` = 0, and 5720 objects for correlation analysis, respectively, in each 0.1×0.2 region on $z - \log L_{\rm bol}$ plane. Objects within the blue dotted square are used to test the influence of the Malmquist bias on correlation analysis (see Section 4.2.2).
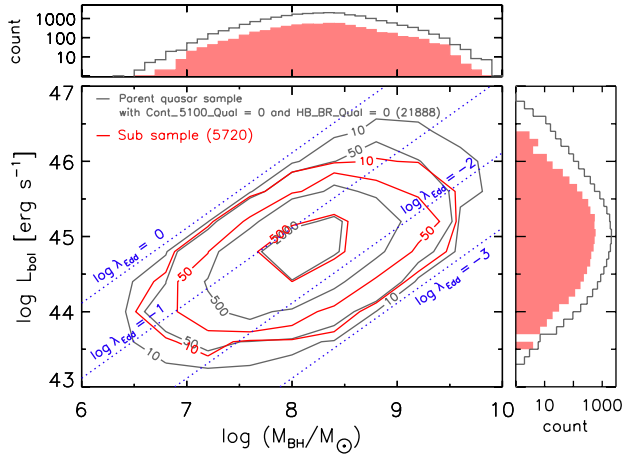
Figure 6. The BH mass and bolometric luminosity of our sample. The histograms of $M_{\rm BH}$ and $L_{\rm bol}$ are attached on the top and right, respectively. The gray and red contours represent the number density of 21,888 objects with `Cont_5100_Qual` = 0 and `HB_BR_Qual` = 0, and 5720 objects for correlation analysis, respectively, in each 0.4×0.4 region on $\log M_{\rm BH} - \log L_{\rm bol}$ plane. The blue diagonal lines show Eddington ratio of $\log \lambda_{\rm Edd} = -3, -2, -1$, and 0 from bottom right to top left.

$\log (M_{\rm BH}/M_\odot)$, and $\log \lambda_{\rm Edd}$ are 45.0 ± 0.46, 8.29 ± 0.45, and -1.41 ± 0.38, respectively.

3.3. Dependences of CF on $L_{\rm bol}$, $M_{\rm BH}$, and $\lambda_{\rm Edd}$

We investigate the dependences of CF on $L_{\rm bol}$, $M_{\rm BH}$, and $\lambda_{\rm Edd}$ of our quasar sample. As mentioned in Sections 3.1 and 3.2, quasars with (i) $\chi^2_{\rm CIGALE} < 3.0$, (ii)

ΔBIC > 6, (iii) $\chi^2_{\rm QSFit} < 3.0$, and (iv) `Cont_5100_Qual` = 0, and (v) `HB_BR_Qual` = 0 are used for the following correlation analysis, which yields 5720 objects (see also Figure 1). We discuss how the above selection cuts affects the dependences of CF in Section 4.2. Their distributions of our sub-sample in $z - L_{\rm bol}$ and $M_{\rm BH} - L_{\rm bol}$ plane are also shown in Figures 5 and 6, respectively. We find that our quasar sample selected from the DR16Q covers $43.5 < \log L_{\rm bol}$ (erg s^{-1}) < 46.4, $6.57 < \log(M_{\rm BH}/M_\odot) < 9.89$, and $-3.16 < \log \lambda_{\rm Edd} < -0.22$. The mean and standard deviation of $\log L_{\rm bol}$ (erg s^{-1}), $\log (M_{\rm BH}/M_\odot)$, and $\log \lambda_{\rm Edd}$ are 45.0 ± 0.39, 8.29 ± 0.46, and -1.41 ± 0.38, respectively. The fact that the DR16Q contains fainter quasars than those in previous releases enables us to investigate the CF for less luminous quasars with less massive BH and smaller accretion rate compared to previous studies baaed on the SDSS quasar catalogs (e.g., Gu 2013; Ma & Wang 2013).

As we cautioned in Section 1, the IR-to-bolometric luminosity ratio would not be always a good tracer of CF. We hence converted from $L_{\rm IR}^{\rm torus}/L_{\rm bol}$ to CF by using a non-liner relation in Stalevski et al. (2016) who provides conversion formula assuming `SKIRTOR` with $R_{\rm max}/R_{\rm min}$ = 30 and $\theta = 0°$ that are the same in Table 1 (see also the middle panel of Figure 7 in Stalevski et al. 2016);

$$\mathrm{CF} = a_4 \left(\frac{L_{\rm IR}^{\rm torus}}{L_{\rm bol}}\right)^4 + a_3 \left(\frac{L_{\rm IR}^{\rm torus}}{L_{\rm bol}}\right)^3$$
$$+ a_2 \left(\frac{L_{\rm IR}^{\rm torus}}{L_{\rm bol}}\right)^2 + a_1 \left(\frac{L_{\rm IR}^{\rm torus}}{L_{\rm bol}}\right) + a_0. \qquad (2)$$

Since we parameterized $\tau_{9.7}$ (see Table 1), we chose $(a_0, a_1, a_2, a_3, a_4) = (0.192478, 1.40827, -1.48727, 0.875215, -0.177798)$, $(0.195615, 1.20218, -1.04546, 0.47493, -0.0601471)$, and $(0.196387, 1.02696, -0.782418, 0.299937, -0.0255416)$ for objects with $\tau_{9.7}$ = 3, 5, and 9, respectively. The uncertainty of CF was propagated from a relative error of $L_{\rm IR}^{\rm torus}/L_{\rm bol}$.

Figure 7 shows the relation between covering factor of dust torus (CF) and AGN properties, i.e., CF–$L_{\rm bol}$, CF–$M_{\rm BH}$, and CF–$\lambda_{\rm Edd}$ for 5720 quasars. We confirm an anti-correlation of the above three quantities, which is consistent with recent works (Ezhikode et al. 2017; Ricci et al. 2017; Zhuang et al. 2018). We also investigate dependence of CF of polar dust (CF$_{\rm PD}$) on $L_{\rm bol}$, $M_{\rm BH}$, and $\lambda_{\rm Edd}$, which is show in Figure 7. We find that CF$_{\rm PD}$ also clearly depend on AGN properties (see Section 4 for quantitative discussion).

4. DISCUSSION

First, we discuss how the AGN polar dust affects the correlation coefficient of dust CF and AGN properties
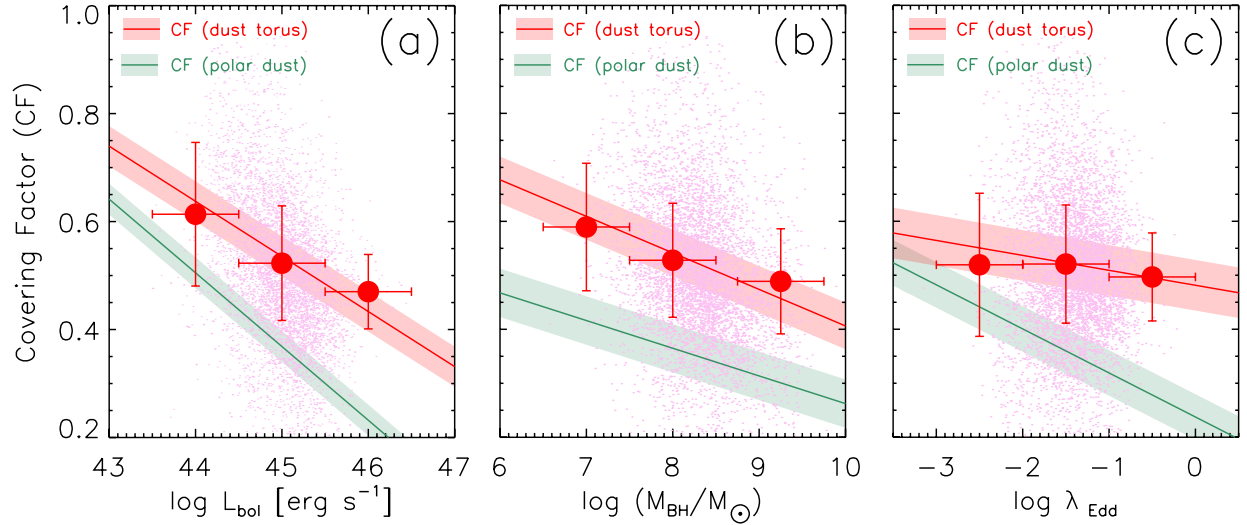
Figure 7. The relation between CF and (a) log L_{bol}, (b) log M_{BH}, and (c) log λ_{Edd} for 5720 quasars at $z < 0.7$. Reddish symbols and lines represent CF of dust torus while green lines represent CF of polar dust. Magenta points represent data while red circles represent weighted mean and standard deviation. Red and green lines with shaded region denote the best-fit relations with 1σ uncertainty.

such as L_{bol}, M_{BH}, and λ_{Edd}. We then argue possible selection effects and uncertainties of CF and correlation analysis through Monte Carlo simulation and mock analysis. Finally, we discuss the dependence of CF–λ_{Edd} correlation on L_{bol}, M_{BH}, and redshift of our sample.

4.1. *Correlation Analysis*

To quantify the anti-correction shown in Figure 7, we conducted a correlation analysis for the sub-sample of 5720 quasars by using a Bayesian maximum likelihood method provided by Kelly (2007), providing a correlation coefficient (r) which takes into account uncertainty on both the x and y values (see e.g., Mateos et al. 2015; Toba et al. 2019a). The same analysis was done for the same sub-sample of 5720 quasars whose CF was derived by the SED fitting without adding the polar dust component in order to check how the presence or absence of polar dust would affect the correlation strength. The resultant correlation coefficients are summarized in Table 3.

Figure 8 shows correlation coefficient (r) of CF–L_{bol}, CF– M_{BH}, and CF–λ_{Edd} with and without adding AGN polar dust component to the SED fitting. We find that the $|r|$ values of objects when considering polar dust emission are larger than those without considering the polar dust. In particular, the influence of the polar dust component on the correlation strength may be significant for CF–λ_{Edd} rather than CF–L_{bol} and CF–M_{BH}. This indicates that polar dust wind, probably driven by radiation pressure from the AGN may be crucial for regulating obscuring dusty structure surrounding SMBHs. Table 3 also provides insight into property of polar dust;

Table 3. Summary of the correlation coefficient (r).

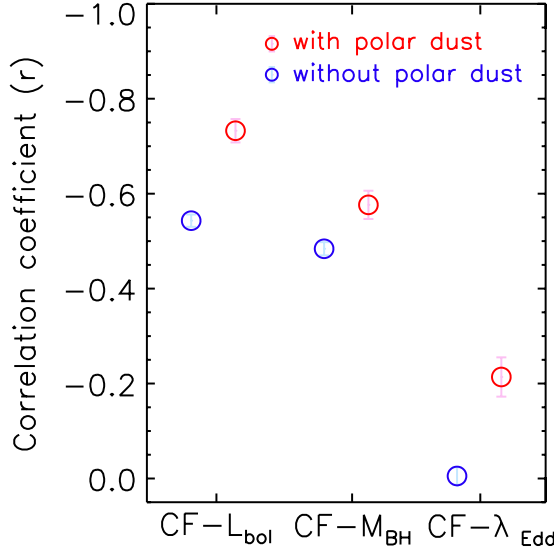|	r without polar dust	r with polar dust
CF –L_{bol}	-0.55 ± 0.01	-0.73 ± 0.02
CF –M_{BH}	-0.48 ± 0.01	-0.58 ± 0.03
CF –λ_{Edd}	-0.01 ± 0.02	-0.21 ± 0.04
$\mathrm{CF_{PD}}$–L_{bol}	—	-0.88 ± 0.01
$\mathrm{CF_{PD}}$–M_{BH}	—	-0.46 ± 0.03
$\mathrm{CF_{PD}}$–λ_{Edd}	—	-0.58 ± 0.02

NOTE—CF and $\mathrm{CF_{PD}}$ denote covering factor of dust torus and polar dust, respectively.

$\mathrm{CF_{PD}}$ seems to strongly depend on L_{bol} and λ_{Edd} rather than M_{BH}, which is consistent with what we discussed the above. Strong radiation pressure from luminous quasars with high λ_{Edd} may blowout dust in polar direction, which would be associate with an AGN-driven outflow (e.g., Schartmann et al. 2014). This suggests that $\mathrm{CF_{PD}}$ is regulated by L_{bol} and possibly λ_{Edd}.

4.2. *Selection Bias*

4.2.1. *Parent SDSS quasar sample*

We used 37,181 quasars at $z < 0.7$ drawn from the SDSS DR16Q as a parent sample (see Figure 1). Since the completeness and contamination rate of the parent sample would directly affect our correlation analysis, we estimate them following Lyke et al. (2020). We utilized 323 objects with `RANDOM_SELECT = 1` that are randomly selected from the DR16Q. This subsample was visually
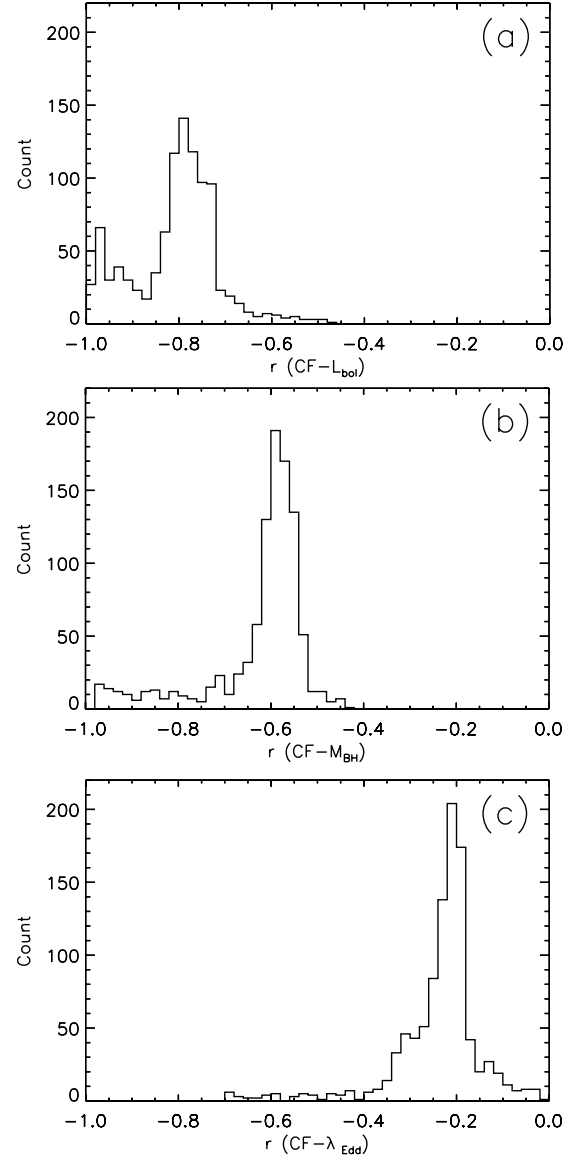
Figure 8. Correlation coefficient (r) of CF–$L_{\rm bol}$, CF–$M_{\rm BH}$, and CF–$\lambda_{\rm Edd}$. r with and without adding AGN polar dust component to the SED fitting are plotted as red and blue color, respectively.

inspected to check whether the pipeline correctly classified the spectrum. If an object is visually confirmed to be a quasar, the object has `IS_QSO_10K = 1`. The confidence rating for a visually identified redshift is stored in `Z_CONF_10K`. We consider objects with `Z_CONF_10K` $\geq$ 2 as those with correct redshift (see Section 3.3 in Lyke et al. 2020, in detail).

The completeness and contamination rate of the parent sample estimated based on Equations (1) and (2) in Lyke et al. (2020) is 99.7% and 0.3%, respectively. This means that the parent quasar sample in this work has quite high completeness and purity, which may not affect our conclusion in this work.

4.2.2. *Malmquist bias*

Because the target selection for quasars was proceeded from flux-limited samples (e.g., Myers et al. 2015), our correlation analysis would be affected by Malmquist bias (see also Figure 5). In order to see how the Malmquist bias would affect the correlation coefficients, we created a sub-sample that is expected not to be affected by the Malmquist bias in which 4785 objects with $44.2 < \log L_{\rm bol} < 45.5$ and $z > 0.3$ were extracted (see a blue dotted square in Figure 5). We then conducted the correlation analysis for the sub-sample in the same manner as what is described in Section 4.1. We find that the mean and standard deviations of r for CF–$L_{\rm bol}$, CF–$M_{\rm BH}$, and CF–$\lambda_{\rm Edd}$ are -0.92 ± 0.05, -0.69 ± 0.10, and -0.30 ± 0.15, respectively. The absolute values of r tend to be higher than what is reported in Table 3 although there are large standard deviations particu-

Figure 9. Simulated distributions of correlation coefficients for (a) CF–$L_{\rm bol}$, (b) CF–$M_{\rm BH}$, and (c) CF–$\lambda_{\rm Edd}$ in which a set of threshold value for sample selection (reduced $\chi^2_{\rm CIGALE}$, reduced $\chi^2_{\rm QSFit}$, and ΔBIC) was randomly chosen (see Section 4.2.3).

larly for $r({\rm CF} - M_{\rm BH})$ and $r({\rm CF} - \lambda_{\rm Edd})$. This result would indicate that Malmquist bias makes the correlation strength weaker.

4.2.3. *Sub-sample of quasars*

As described in Sections 3.1 and 3.2, we created a sub-sample for the correlation analysis by considering the reduced $\chi^2_{\rm CIGALE}$, $\chi^2_{\rm QSFit}$, ΔBIC, `Cont_5100_Qual`, and `HB_BR_Qual` to understand how AGN polar dust affects dust CF. In particular, the threshold of ΔBIC contributed to a decrease in the sample size of quasars from 37,181 to 5720, although the number of the sample is still

enough for statistical investigation. We discuss how the selection criteria for the correlation analysis would be biased toward the resultant correlation coefficient. To address this issue, we performed a Monte Carlo simulation in which we randomly chose a set of threshold value (reduced χ^2_{CIGALE}, reduced χ^2_{QSFit}, and $\Delta\mathrm{BIC}$), and conducted the correlation analysis. We iterated the above process 1000 times where calculation was executed only if the sample size exceeds 1000 in order to insure a reliability of resultant correlation coefficient.

Figure 9 shows the distribution of r. The mean and standard deviations of r for CF–L_{bol}, CF–M_{BH}, and CF–λ_{Edd} are -0.80 ± 0.09, -0.62 ± 0.10 and -0.23 ± 0.10, respectively, which are roughly consistent with what we obtained in this work (see Table 3). This suggests that selection bias caused by adopting threshold values in this work does not significantly affect the result of the correlation analysis.

4.3. Influence of a limited number of stellar templates on the correlation coefficients

For the SED and spectral fitting in a consistent manner, we fixed the age of the main stellar population to be 5.0 Gyr for the SED fitting while we used the template of an elliptical galaxy with a stellar age of 5.0 Gyr for the spectral fitting (see Sections 2.3 and 2.4). Although this assumption (i.e., low-z quasars are hosted by elliptical galaxies) is expected to apply to the majority of our quasar sample (e.g., Bahcall et al. 1997; Dunlop et al. 2003; Kauffmann et al. 2003; Floyd et al. 2004), a fraction of quasars could not be the case (e.g., McLure et al. 1999; Schawinski et al. 2010; Ishino et al. 2020). How do these possible variations of quasar host properties would affect resulting correlation coefficients?

To address this issue, we modified (i) the parameter ranges in the age of the main stellar population used for the SED fitting and (ii) AGN host templates for the spectral fitting. For the SED fitting, we allowed the age of the main stellar population to vary from 1.0 to 11.0 Gyr at intervals of 2.0 Gyr. For the spectral fitting, we utilized host galaxy templates of a simulated 2.0 Gyr old elliptical galaxy, S0-galaxy, and three types of spiral galaxies (i.e., Sa, Sb, and Sc) (Polletta et al. 2007), in addition to the 5.0 Gyr old elliptical galaxy template we originally used. We randomly chose a host galaxy template from the above options. We then performed the SED fitting and spectral fitting in the same manner as what is described in Sections 2.3 and 2.4. We iterated this process 1000 times and estimate the distribution of r.

The resulting distributions of r are shown in Figure 10. We find that the mean and standard deviations of r
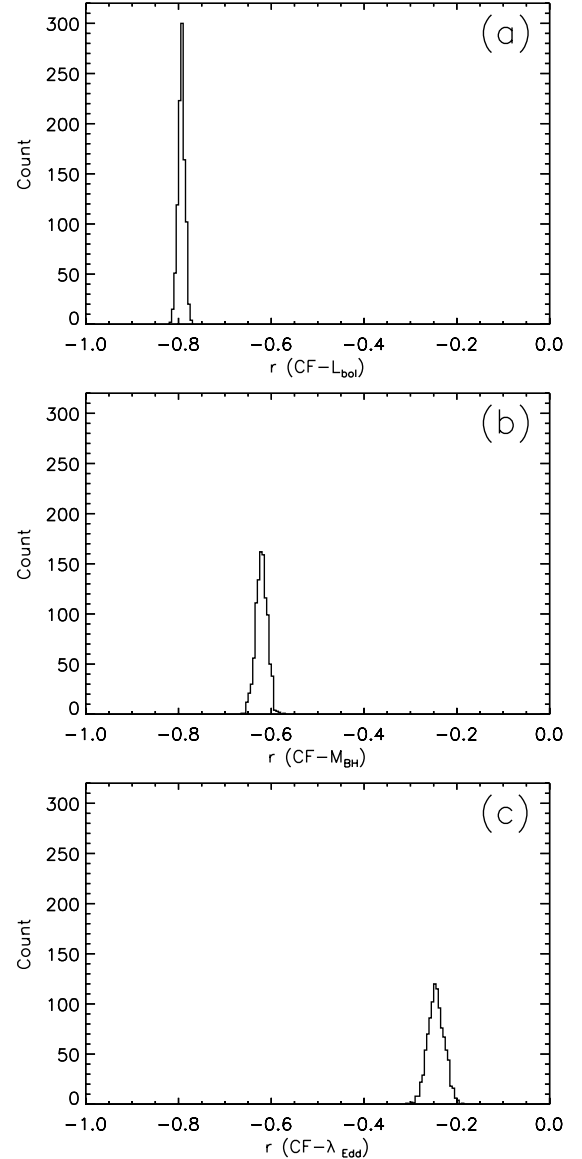
Figure 10. Simulated distributions of correlation coefficients for (a) CF–L_{bol}, (b) CF–M_{BH}, and (c) CF–λ_{Edd} in which stellar template for spectral fitting was randomly chosen (see Section 4.3).

for CF–L_{bol}, CF–M_{BH}, and CF–λ_{Edd} are -0.79 ± 0.00, -0.62 ± 0.01, and -0.24 ± 0.01, respectively, which are in good agreement with what we obtained in this work (see Table 3). Therefore, we conclude that the influence of a limited number of stellar templates on the correlation coefficients is likely to be small.

4.4. Influence of CF–L_{bol} correlation on CF–λ_{Edd} correlation coefficient

We reported in Section 4.1 that CF depends on λ_{Edd} by taking into account polar dust emission. It should be noted that λ_{Edd} is directly related to L_{bol} that strongly

correlates with CF, which would induce an artificial correlation of CF–λ_{Edd}.

To disentangle the dependence and see how r (CF–λ_{Edd}) would be affected by strong correlation of CF–L_{bol}, we employed a diagnostic method presented in Hasinger (2008) who investigated redshift dependence on CF based on the relation between the CF and X-ray luminosity (see also Toba et al. 2014). First, we estimated the average value of the slope of the relation between the CF and L_{bol} in the range of $-2.0 <$ log $\lambda_{\mathrm{Edd}} < 0.0$. We then estimated the normalization value at a luminosity of log $L_{\mathrm{bol}} = 45.0$ erg s^{-1}, in the middle of the observed range, as a function of the λ_{Edd} by keeping the slope fixed to the average value. The λ_{Edd} bins were $-2.0 <$ log $\lambda_{\mathrm{Edd}} < -1.5$, $-1.5 <$ log $\lambda_{\mathrm{Edd}} < -1.0$, $-1.0 <$ log $\lambda_{\mathrm{Edd}} < -0,5$, and $-0.5 <$ log $\lambda_{\mathrm{Edd}} < 0.0$ in the range of log $L_{\mathrm{bol}} = 44$–46 erg s^{-1}. We find that the resulting correlation coefficient is r (CF–λ_{Edd}) ~ 0.25, which is consistent with what we obtained in Section 4.1. Therefore, we conclude that a strong CF–L_{bol} correlation may not significantly affect the correlation coefficient of CF–λ_{Edd}.
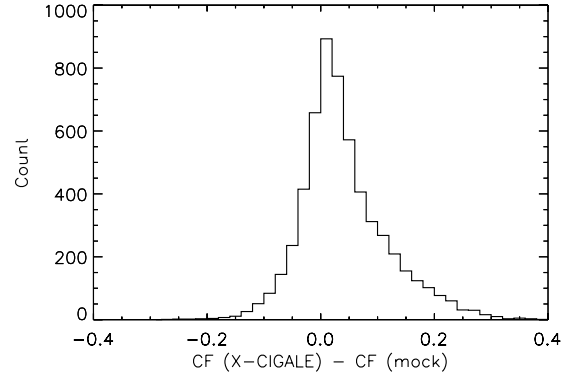
4.5. Mock Analysis

Finally, we check whether or not the derived CF can actually be estimated reliably, given the limited number of photometry and its uncertainty. We execute a mock analysis that is a procedure provided by X-CIGALE (see e.g., Buat et al. 2012, 2014; Ciesla et al. 2015; Lo Faro et al. 2017; Boquien et al. 2019; Toba et al. 2019b, 2020c, for more detail) for 5720 quasars. This analysis is done by a mock catalog in which a value is taken from a Gaussian distribution with the same standard deviation as the observation is added to each photometry originally used, which would also enable to test how the difference in photometry influences CF (see Section 2.3).

Figure 11 shows the histogram of differences in CFs that are derived from X-CIGALE in this work and from the mock catalog. The mean and standard deviations of $\Delta \mathrm{CF} = 0.04 \pm 0.07$, suggesting that CF of majority of our quasar sample is insensitive to the limited number of photometric points and difference in photometry.

4.6. Influence of AGN properties on CF–λ_{Edd} Correlation

In section 4.1, we report that adding AGN polar dust emission to SED fitting makes anti-correlations of CF–L_{bol}, CF–M_{BH}, and CF–λ_{Edd} more stronger than those without adding it. On the other hand, L_{bol}, M_{BH}, λ_{Edd}, and also redshift should be correlated with each other as mentioned in Sections 4.2.2 and 4.4 (see also Figures

Figure 11. Histogram of difference in CFs that are derived in this work and from mock analysis for 5720 quasars.

Table 4. Dependence of correlation coefficient of CF–λ_{Edd} on redshift, BH mass, and bolometric luminosity.

	Parameter Range	r (CF–λ_{Edd})
	$z < 0.1$	-0.33 ± 0.45
Redshift	$0.1 < z < 0.2$	-0.25 ± 0.13
	$z > 0.2$	-0.22 ± 0.05
	$\log (M_{\mathrm{BH}}/M_\odot) < 8$	-0.55 ± 0.07
BH mass	$8 < \log (M_{\mathrm{BH}}/M_\odot) < 9$	-0.49 ± 0.04
	$\log (M_{\mathrm{BH}}/M_\odot) > 10$	-0.45 ± 0.21
	$\log L_{\mathrm{bol}} > 44.0$	-0.12 ± 0.10
L_{bol} (erg s^{-1})	$44 < \log L_{\mathrm{bol}} < 45.0$	-0.07 ± 0.12
	$\log L_{\mathrm{bol}} > 45.0$	0.05 ± 0.06

NOTE—Polar dust component is taken into account to estimate r (CF–λ_{Edd}).

5 and 6). With all the caveats discussed in Sections 4.2 – 4.5 in mind, we discuss how CF–λ_{Edd} correlation depends on AGN properties (i.e., L_{bol} and M_{BH}) and redshift. The resultant correlation coefficients are summarized in Table 4.

4.6.1. Redshift Dependence

Although we confirm that anti-correlations of CF and L_{bol}, M_{BH}, and λ_{Edd}, the correlation strength differs among them. We find that CF–L_{bol} correlation is stronger than other two correlations as shown in Table 3 and Figure 8, which seems inconsistent with X-ray based work (Ricci et al. 2017) who reported that CF–λ_{Edd} correlation is stronger than CF–L_{bol} correlation. What causes this discrepancy?

There are some possibilities such as the difference in (i) redshift, (ii) sample selection (i.e., our sample is limited to type 1 quasars while sample in Ricci et al. 2017 is not the case), and (iii) definition of CF (i.e.,
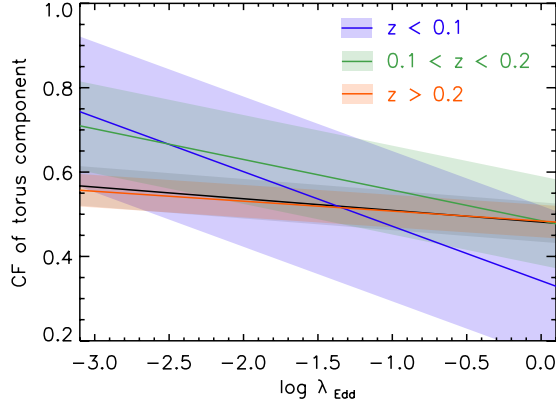
Figure 12. The CF as a function of λ_{Edd}. The blue, green, orange, and gray shaded region represent quasars with $z < 0.1$, $0.1 < z < 0.2$, and $z > 0.2$, and all sample, respectively.
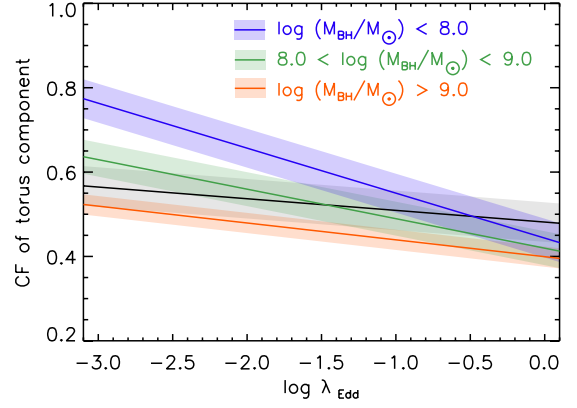

Figure 13. The CF as a function of λ_{Edd}. The blue, green, orange, and gray shaded region represent quasars with $\log\,(M_{\mathrm{BH}}/M_\odot) < 8$, $8 < \log\,(M_{\mathrm{BH}}/M_\odot) < 9$, $\log\,(M_{\mathrm{BH}}/M_\odot) > 9$, and all sample, respectively.

$L_{\mathrm{IR}}^{\mathrm{torus}}/L_{\mathrm{bol}}$ is employed in this work while fraction of obscured sources is employed in Ricci et al. 2017). It is hard to quantify, however, the influence of the difference in the sample selection and definition of CF on the correlation strength and is beyond the scope of this work. We thus argue that a possibility that the difference in redshift would cause the discrepancy. Ricci et al. (2017) targeted nearby AGNs with a median redshift of $z \sim 0.037$ whereas we focus on AGNs with much higher redshift up to $z = 0.7$.

Figure 12 shows redshift dependence of CF–λ_{Edd} relation. We find that CF of AGNs with $z < 0.1$ (that is similar to that of sample in Ricci et al. (2017)) tends to strongly depend on λ_{Edd}, with a correlation coefficient of $r = -0.33 \pm 0.45$ while CF–λ_{Edd} for AGNs at $z > 0.2$ shows weaker correlations than what at $z < 0.1$. This indicates that the aforementioned discrepancy can be explained by difference in redshift of sample between Ricci et al. (2017) and this work. We also remind that our correlation analysis would be affected by the Malmquist bias, which could make the correlation strength weaker, as discussed in Section 4.2.2.

This result also might suggest that CF decreases with increasing redshift at least $z < 0.7$, trend of which is consistent with what is reported in Toba et al. (2014) although there is large uncertainty. On the other hand, the fraction of obscured X-ray AGNs increases with redshift for the same luminosity (e.g., Ueda et al. 2014). This discrepancy might be caused by difference in sample selection and definition of CF.

4.6.2. BH Mass Dependence

Recently, Kawakatu et al. (2020) constructed a model of a nuclear starburst disk supported by the turbulent pressure from SNe II and investigated how CF depends on AGN properties by taking account anisotropic radia-

tion pressure from AGNs. They found that CF strongly depend on λ_{Edd} for AGNs with $M_{\mathrm{BH}} < 10^8\,M_\odot$ while the dependence of CF on λ_{Edd} is much weaker for AGNs with $M_{\mathrm{BH}} > 10^{9-10}\,M_\odot$. Although they did not incorporate the AGN polar dust outflow, it is worth checking the dependence of CF–λ_{Edd} correlation on M_{BH}. Figure 13 shows how the difference in M_{BH} would affect on the correlation strength of CF–λ_{Edd}. The resultant r of CF–λ_{Edd} for quasars with $\log\,(M_{\mathrm{BH}}/M_\odot) < 8$, $8 < \log\,(M_{\mathrm{BH}}/M_\odot) < 9$, and $\log\,(M_{\mathrm{BH}}/M_\odot) > 9$ are -0.55 ± 0.07, -0.49 ± 0.04, and -0.45 ± 0.21, respectively. This result indicates that CF of quasar with $< 10^8\,M_\odot$ strongly depends on λ_{Edd}. The overall statistical trend is in good agreement with what reported in Kawakatu et al. (2020).

4.6.3. Bolometric Luminosity Dependence

Figure 14 shows dependence of L_{bol} on CF–λ_{Edd}. We find that anti-correlation of CF–λ_{Edd} may disappear for AGNs with $\log L_{\mathrm{bol}} > 45.0$. In this L_{bol} range, the correlation coefficients are even positive with large uncertainty (see Table 4). Zhuang et al. (2018) reported that CF of luminous quasars with $L_{\mathrm{bol}} \gtrsim 10^{45.0}$ erg s^{-1} increases with increasing λ_{Edd}, although this positive correlation would appear when $\log \lambda_{\mathrm{Edd}}$ ranges from -0.25 and 0.5. This result could indicate that overall trend of CF–λ_{Edd} reported in Section 4.1 is determined by AGNs with $44.0 < L_{\mathrm{bol}} < 45.0$.

5. SUMMARY

In this paper, we revisit the relationship between the CF and AGN properties (L_{bol}, M_{BH}, and λ_{Edd}) for type 1 quasars selected from the SDSS DR16 quasar catalog. Thanks to the newly available DR16Q, we can investigate the dependence of CF for quasars with a wide
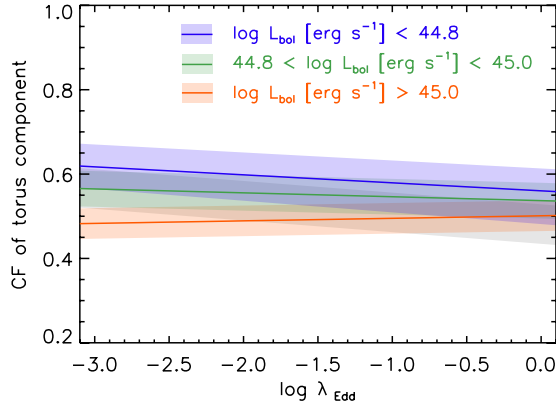
Figure 14. The CF as a function of $\lambda_{\rm Edd}$. The blue, green, orange, and gray shaded region represent quasars with log $L_{\rm bol} < 44.8$, $44.8 < $ log $L_{\rm bol} < 45.0$, log $L_{\rm bol} > 45.0$, and all sample, respectively.

range in $L_{\rm bol}$, $M_{\rm BH}$, and $\lambda_{\rm Edd}$. We narrowed down the DR16Q catalog to 37,181 quasars with $z < 0.7$, and performed the SED fitting with X-CIGALE to at most 13 optical–MIR photometry and spectral fitting with QSFit to the SDSS spectra. In particular, we took into account the contribution of AGN polar dust emission to IR luminosity, which could affect the measurement of CF. For 5720 quasars whose physical quantities estimated by X-CIGALE and QSFit are reliable, we conducted a correlation analysis to see how the AGN polar dust would affect the correlation coefficient. We find that taking intro account the contribution of AGN polar dust to IR emission provides stronger anti-correlations of CF–$L_{\rm bol}$, CF–$M_{\rm BH}$, and CF–$\lambda_{\rm Edd}$ than not considering the polar dust. This result indicates that AGN polar dust wind is a key ingredient to regulate the obscuring structure of AGNs.

Facilities: Sloan, CTIO:2MASS, FLWO:2MASS, UKIRT, *WISE*

Software: IDL, IDL Astronomy User's Library (Landsman 1993), X-CIGALE (Boquien et al. 2019; Yang et al. 2020), QSFit (Calderone et al. 2017), TOPCAT (Taylor 2006).

APPENDIX

A. A VALUE-ADDED CATALOG FOR SDSS DR16 QUASARS AT $Z < 0.7$

We provide physical properties of 37,181 quasars at $z < 0.7$ selected from the SDSS DR16Q. The catalog description is summarized in Table 2.

Table 2. Physical properties of 37,181 quasars at $z < 0.7$ selected from the SDSS DR16.

Column name	Format	Unit	Description
SpecObjID	LONG		Unique id in the SDSS DR16
Plate	INT32		Spectroscopic plate number
MJD	INT32		Modified Julian day of the spectroscopic observation
FiberID	INT16		Fiber ID number
R.A.	DOUBLE	degree	Right Assignation (J2000.0) from the SDSS DR16Q
Decl.	DOUBLE	degree	Declination (J2000.0) from the SDSS DR16Q
Redshift	DOUBLE		Redshift (that is taken from a column, "Z" in the SDSS DR16Q)
rechi2_QSFIT	DOUBLE		Reduced χ^2 derived from `QSFIT`
Cont_L3000	DOUBLE	erg s^{-1}	AGN continuum luminosity at the rest-frame 3000 Å derived from `QSFIT`
Cont_L3000_err	DOUBLE	erg s^{-1}	Uncertainty of Cont_L3000 derived from `QSFIT`
Slope_3000	DOUBLE		AGN continuum slope at the rest-frame 3000 Å derived from `QSFIT`
Slope_3000_err	DOUBLE		Uncertainty of Slope_3000 derived from `QSFIT`
Cont_3000_Qual	INT32		Quality flag of continuum at the rest-frame 3000 Å derived from `QSFIT`
			(see Appendix A (xix) in Calderone et al. 2017)
Cont_L5100	DOUBLE	erg s^{-1}	AGN continuum luminosity at the rest-frame 5100 Å derived from `QSFIT`
Cont_L5100_err	DOUBLE	erg s^{-1}	Uncertainty of Cont_L5100 derived from `QSFIT`
Slope_5100	DOUBLE		AGN continuum slope at the rest-frame 5100 Å derived from `QSFIT`
Slope_5100_err	DOUBLE		Uncertainty of Slope_5100 derived from `QSFIT`
Cont_5100_Qual	INT32		Quality flag of continuum at the rest-frame 5100 Å derived from `QSFIT`
			(see Appendix A (xix) in Calderone et al. 2017)
Lum_MgII	DOUBLE	erg s^{-1}	Line luminosity of Mg II derived from `QSFIT`
Lum_MgII_err	DOUBLE	erg s^{-1}	Uncertainty of Lum_MgII derived from `QSFIT`
FWHM_MgII	DOUBLE	km s^{-1}	FWHM of Mg II derived from `QSFIT`
FWHM_MgII_err	DOUBLE	km s^{-1}	Uncertainty of FWHM_MgII derived from `QSFIT`
EW_MgII	DOUBLE	Å	Equivalent width of Mg II derived from `QSFIT`
EW_MgII_err	DOUBLE	Å	Uncertainty of EW_MgII derived from `QSFIT`
MgII_Qual	INT32		Quality flag of Mg II line derived from `QSFIT`
			(see Appendix A (xxxvi) in Calderone et al. 2017)
Lum_HB_BR	DOUBLE	erg s^{-1}	Line luminosity of Hβ (broad component) derived from `QSFIT`
Lum_HB_BR_err	DOUBLE	erg s^{-1}	Uncertainty of Lum_HB_BR derived from `QSFIT`
FWHM_HB_BR	DOUBLE	km s^{-1}	FWHM of Hβ (broad component) derived from `QSFIT`
FWHM_HB_BR_err	DOUBLE	km s^{-1}	Uncertainty of FWHM_HB_BR derived from `QSFIT`
EW_HB_BR	DOUBLE	Å	Equivalent width of Hβ (broad component) derived from `QSFIT`
EW_HB_BR_err	DOUBLE	Å	Uncertainty of EW_HB_BR derived from `QSFIT`

Table 2 *continued*

Table 2 *(continued)*

Column name	Format	Unit	Description
HB_BR_Qual	INT32		Quality flag of Hβ (broad component) line derived from QSFIT
			(see Appendix A (xxxvi) in Calderone et al. 2017)
Lum_HB_NA	DOUBLE	erg s^{-1}	Line luminosity of Hβ (narrow component) derived from QSFIT
Lum_HB_NA_err	DOUBLE	erg s^{-1}	Uncertainty of Lum_HB_NA derived from QSFIT
FWHM_HB_NA	DOUBLE	km s^{-1}	FWHM of Hβ (narrow component) derived from QSFIT
FWHM_HB_NA_err	DOUBLE	km s^{-1}	Uncertainty of FWHM_HB_NA derived from QSFIT
EW_HB_NA	DOUBLE	Å	Equivalent width of Hβ (narrow component) derived from QSFIT
EW_HB_NA_err	DOUBLE	Å	Uncertainty of EW_HB_NA derived from QSFIT
HB_NA_Qual	INT32		Quality flag of Hβ (narrow component) line derived from QSFIT
			(see Appendix A (xxxvi) in Calderone et al. 2017)
Lum_OIII_NA	DOUBLE	erg s^{-1}	Line luminosity of [O III]λ5007 (narrow component) derived from QSFIT
Lum_OIII_NA_err	DOUBLE	erg s^{-1}	Uncertainty of Lum_HB_NA derived from QSFIT
FWHM_OIII_NA	DOUBLE	km s^{-1}	FWHM of [O III]λ5007 (narrow component) derived from QSFIT
FWHM_OIII_NA_err	DOUBLE	km s^{-1}	Uncertainty of FWHM_OIII_NA derived from QSFIT
EW_OIII_NA	DOUBLE	Å	Equivalent width of [O III]λ5007 (narrow component) derived from QSFIT
EW_OIII_NA_err	DOUBLE	Å	Uncertainty of EW_OIII_NA derived from QSFIT
OIII_NA_Qual	INT32		Quality flag of [O III]λ5007 (narrow component) line derived from QSFIT
			(see Appendix A (xxxvi) in Calderone et al. 2017)
Lum_OIII_BW	DOUBLE	erg s^{-1}	Line luminosity of [O III]λ5007 (blue wing component) derived from QSFIT
Lum_OIII_BW_err	DOUBLE	erg s^{-1}	Uncertainty of Lum_HB_BW derived from QSFIT
FWHM_OIII_BW	DOUBLE	km s^{-1}	FWHM of [O III]λ5007 (blue wing component) derived from QSFIT
FWHM_OIII_BW_err	DOUBLE	km s^{-1}	Uncertainty of FWHM_OIII_BW derived from QSFIT
EW_OIII_BW	DOUBLE	Å	Equivalent width of [O III]λ5007 (blue wing component) derived from QSFIT
EW_OIII_BW_err	DOUBLE	Å	Uncertainty of EW_OIII_BW derived from QSFIT
Voff_OIII_BW	DOUBLE	km s^{-1}	Velocity offset of [O III]λ5007 (blue wing component) derived from QSFIT
Voff_OIII_BW_err	DOUBLE	km s^{-1}	Uncertainty of Voff_OIII_BW derived from QSFIT
OIII_BW_Qual	INT32		Quality flag of [O III]λ5007 (blue wing component) line derived from QSFIT
			(see Appendix A (xxxvi) in Calderone et al. 2017)
Lum_HA_BR	DOUBLE	erg s^{-1}	Line luminosity of Hβ (broad component) derived from QSFIT
Lum_HA_BR_err	DOUBLE	erg s^{-1}	Uncertainty of Lum_HA_BR derived from QSFIT
FWHM_HA_BR	DOUBLE	km s^{-1}	FWHM of Hα (broad component) derived from QSFIT
FWHM_HA_BR_err	DOUBLE	km s^{-1}	Uncertainty of FWHM_HA_BR derived from QSFIT
EW_HA_BR	DOUBLE	Å	Equivalent width of Hα (broad component) derived from QSFIT
EW_HA_BR_err	DOUBLE	Å	Uncertainty of EW_HA_BR derived from QSFIT
HA_BR_Qual	INT32		Quality flag of Hα (broad component) line derived from QSFIT
			(see Appendix A (xxxvi) in Calderone et al. 2017)
Lum_HA_NA	DOUBLE	erg s^{-1}	Line luminosity of Hβ (narrow component) derived from QSFIT
Lum_HA_NA_err	DOUBLE	erg s^{-1}	Uncertainty of Lum_HA_NA derived from QSFIT
FWHM_HA_NA	DOUBLE	km s^{-1}	FWHM of Hα (narrow component) derived from QSFIT
FWHM_HA_NA_err	DOUBLE	km s^{-1}	Uncertainty of FWHM_HA_NA derived from QSFIT
EW_HA_NA	DOUBLE	Å	Equivalent width of Hα (narrow component) derived from QSFIT

Table 2 continued

Table 2 *(continued)*

Column name	Format	Unit	Description
EW_HA_NA_err	DOUBLE	Å	Uncertainty of EW_HA_BR derived from QSFIT
HA_NA_Qual	INT32		Quality flag of Hα (narrow component) line derived from QSFIT
			(see Appendix A (xxxvi) in Calderone et al. 2017)
log_MBH	DOUBLE	$M_\odot$	Black hole mass (see Equation 1)
log_MBH_err	DOUBLE	$M_\odot$	Uncertainty of log_MBH
log_Lbol	DOUBLE	erg s^{-1}	Bolometric luminosity (see Section 2.4)
log_Lbol_err	DOUBLE	erg s^{-1}	Uncertainty of log_Lbol
log_lambda_Edd	DOUBLE		Eddington ratio
log_lambda_Edd_err	DOUBLE		Uncertainty of log_lambda_Edd
rechi2_XCIGALE	DOUBLE		Reduced χ^2 derived from X-CIGALE
Delta_BIC	DOUBLE		$\text{BIC}_{\text{wopolar}} - \text{BIC}_{\text{wpolar}}$ (see Section 3.1)
E_BV	DOUBLE		Color excess ($E(B-V)$) derived from X-CIGALE
E_BV_err	DOUBLE		Uncertainty of color excess ($E(B-V)$) derived from X-CIGALE
log_M	DOUBLE	$M_\odot$	Stellar mass derived from X-CIGALE
log_M_err	DOUBLE	$M_\odot$	Uncertainty of stellar mass derived from X-CIGALE
log_SFR	DOUBLE	$M_\odot$ yr^{-1}	SFR derived from X-CIGALE
log_SFR_err	DOUBLE	$M_\odot$ yr^{-1}	Uncertainty of SFR derived from X-CIGALE
log_LIR	DOUBLE	$L_\odot$	IR luminosity derived from X-CIGALE
log_LIR_err	DOUBLE	$L_\odot$	Uncertainty of IR luminosity derived from X-CIGALE
log_LIR_AGN	DOUBLE	$L_\odot$	IR luminosity contributed from AGN derived from X-CIGALE
log_LIR_AGN_err	DOUBLE	$L_\odot$	Uncertainty of log_LIR_AGN derived from CIGALE
log_LIR_AGN_polar	DOUBLE	erg s^{-1}	IR luminosity contributed from AGN polar dust component
			derived from CIGALE
log_LIR_AGN_polar_err	DOUBLE	erg s^{-1}	Uncertainty of log_LIR_polar derived from CIGALE
log_LIR_AGN_torus	DOUBLE	erg s^{-1}	IR luminosity contributed from AGN dust torus component
			derived from CIGALE
log_LIR_AGN_torus_err	DOUBLE	erg s^{-1}	Uncertainty of log_LIR_torus derived from CIGALE
CF_AGN_torus	DOUBLE		Covering factor of AGN dust torus (see Equation 2)
CF_AGN_torus_err	DOUBLE		Uncertainty of CF_AGN_torus

NOTE—5720 quasars with $(\chi^2/\text{dof})_{\text{QSFit}} < 3.0$, $(\chi^2/\text{dof})_{\text{CIGALE}} < 3.0$, $\Delta\text{BIC} > 6$, Cont_5100_Qual $= 0$, and HB_BR_Qual $= 0$ are used for a correlation analysis (see Section 3.3). This table is available in its entirety in a machine-readable form in the online journal.

REFERENCES

Aihara, H., Allende Prieto, C., An, D., et al. 2011, ApJS, 193, 29

Alonso-Herrero, A., Ramos Almeida, C., Mason, R., et al. 2011, ApJ, 736, 82

Antonucci, R. 1993, ARA&A, 31, 473

Asmus, D. 2019, MNRAS, 489, 2177

Aufort, G., Ciesla, L, Pudlo, P., & Buat, V. 2020, A&A, 635, A136

Baba, S., Nakagawa, T., Isobe, N., & Shirahata, M. 2018, ApJ, 852, 83

Bahcall, J. N., Kirhakos, S., Saxe, D. H., & Schneider, D. P. 1997, ApJ, 479, 642

Baloković, M., Brightman, M., Harrison, F. A., et al. 2018, ApJ, 854, 42

Baes, M., Verstappen, J., de Looze, I., et al. 2011, ApJS, 196, 22

Bolton, A. S., Schlegel, D. J., Aubourg, É., et al. 2012, AJ, 144, 144

Boquien, M., Buat, V., & Perret, V. 2014, A&A, 571, A72

Boquien, M., Kennicutt, R., Calzetti, D., et al. 2016, A&A, 591, A6

Boquien, M., Burgarella, D., Roehlly, Y., et al. 2019, A&A, 622, A103

Brightman, M., Baloković, M., Stern, D., et al. 2015, ApJ, 805, 41

Bruzual, G., & Charlot, S. 2003, MNRAS, 344, 1000

Buat, V., Ciesla, L., Boquien, M., Małek, K., & Burgarella, D. 2019, A&A, 632, A79

Buat, V., Heinis, S., Boquien, M., et al. 2014, A&A, 561, A39

Buat, V., Noll, S., Burgarella, D., et al. 2012, A&A, 545, A141

Buat, V., Oi, N., Heinis, S., et al. 2015, A&A, 577, A141

Burgarella, D., Buat, V., & Iglesias-Páramo, J. 2005, MNRAS, 360, 1413

Burgarella D., Nanni A., Hirashita H., et al. 2020, A&A, 637, A32

Burlon, D., Ajello, M., Greiner, J., et al. 2011, ApJ, 728, 58

Camps, P., & Baes, M. 2015, A&C, 9, 20

Calderone, G., Nicastro, L., Ghisellini, G., et al. 2017, MNRAS, 472, 4051

Cao, X. 2005, ApJ, 619, 86

Casey, C. M. 2012, MNRAS, 425, 3094

Chabrier, G. 2003, PASP, 115, 763

Charlot, S., & Fall, S. M. 2000, ApJ, 539, 718

Ciesla, L., Charmandaris, V., Georgakakis, A., et al. 2015, A&A, 576, A10

Ciesla, L., Boselli, A., Elbaz, D., et al. 2016, A&A, 585, A43

Ciesla, L., Elbaz, D., & Fensch, J. 2017, A&A, 608, A41

Ciesla, L., Elbaz, D., Schreiber, C., Daddi, E., & Wang, T. 2018, A&A, 615, A61

Coffey, D., Salvato, M., Merloni, A., et al. 2019, A&A, 625, A123

Cutri, R. M., Wright, E. L., Conrow, T., et al. 2014, yCat, 2328, 0

Dietrich M., Appenzeller I., Vestergaard M., Wagner S. J., 2002, ApJ, 564, 581

Draine, B. T. 2006, ApJ, 636, 1114

Dunlop, J. S., McLure, R. J., Kukula, M. J., et al. 2003, MNRAS, 340, 1095

Dwelly, T., & Page, M. J. 2006, MNRAS, 372, 1755

Ezhikode S. H., Gandhi P., Done C., et al. 2017, MNRAS, 472, 3492

Floyd, D. J. E., Kukula, M. J., Dunlop, J. S., et al. 2004, MNRAS, 355, 196

Fritz, J., Franceschini, A., & Hatziminaoglou, E. 2006, MNRAS, 366, 767

Grandi S. A., 1982, ApJ, 255, 25

Gandhi, P., Hönig, S. F., & Kishimoto, M. 2015, ApJ, 812, 113

Gandhi, P., Horst, H., Smette, A., et al. 2009, A&A, 502, 457

Gu, M. 2013, ApJ, 773, 176

Hasinger, G. 2008, A&A, 490, 905

Hickox, R. C., & Alexander, D. M. 2018, ARA&A, 56, 625

Hönig, S. F., Kishimoto, M., Tristram, K. R. W., et al. 2013, ApJ, 771, 87

Hönig, S. F. 2019, ApJ, 884, 171

Ichikawa, K., Ricci, C., Ueda, Y., et al. 2019, ApJ, 870, 31

Imanishi, M., Nakanishi, K., & Izumi, T. 2016, ApJL, 822, L10

Imanishi, M., Nakanishi, K., & Izumi, T. 2018, ApJL, 853, L25

Inoue, A. K. 2011, MNRAS, 415, 2920

Ishino, T., Matsuoka, Y., Koyama, S., et al. 2020, PASJ, 72, 83

Izumi, T., Wada, K., Fukushige, R., Hamamura, S., & Kohno, K. 2018, ApJ, 867, 48

Jaffe, W., Meisenheimer, K., Röttgering, H. J. A., et al. 2004, Nature, 429, 47

Kauffmann, G., Heckman, T. M., Tremonti, C., et al. 2003, MNRAS, 346, 1055

Kawakatu, N., & Wada, K. 2008, ApJ, 681, 73

Kawakatu, N., Wada, K., & Ichikawa, K. 2020, ApJ, 889, 84

Kelly, B. C., 2007, ApJ, 665, 1489

Kishimoto, M., Hönig, S. F., Antonucci, R., et al. 2011, A&A, 527, A121

Krolik, J. H., & Begelman, M. C. 1986, ApJL, 308, L55

Kuhn O., Elvis M., Bechtold J., Elston R., 2001, ApJS, 136, 225

Lo Faro, B., Buat, V., Roehlly, Y., et al. 2017, MNRAS, 472, 1372

La Franca, F., Fiore, F., Comastri, A., et al. 2005, ApJ, 635, 864

Landsman, W. B. 1993, in ASP Conf. Ser. 52, Astronomical Data Analysis Software and Systems II, ed. R. J. Hanisch, R. J. V. Brissenden, & J. Barnes (San Francisco, CA: ASP), 246

Lang, D. 2014, AJ, 147, 108,

Lang, D., Hogg, D. W., & Schlegel, D. J. 2016, AJ, 151, 36

Law, N. M., Kulkarni, S. R., Dekany, R. G., et al. 2009, PASP, 121, 1395

Lawrence, A., Warren, S. J., Almaini, O., et al. 2007, MNRAS, 379, 1599

Lawrence, A., & Elvis, M. 2010, ApJ, 714, 561

Leftley, J. H., Tristram, K. R. W., Hönig, S. F., et al. 2018, ApJ, 862, 17

Liddle, A. R. 2004, MNRAS, 351, L49

López-Gonzaga, N., Burtscher, L., Tristram, K. R. W., et al. 2016, A&A, 591, A47

Lyu J., & Rieke G. H., 2018, ApJ, 866, 92

Lyke, B. W., Higley, A. N., McLane, J. N., et al. 2020, ApJS, 250, 8

Ma, X.-C., & Wang, T.-G. 2013, MNRAS, 430, 3445

Maiolino, R., Shemmer, O., Imanishi, M., et al. 2007, A&A, 468, 979

Marchesi S., Ajello M., Zhao X., et al. 2019, ApJ, 882, 162

Markwardt, C. B. 2009, in ASP Conf. Ser. 411, Astronomical Data Analysis Software and Systems XVIII, 411, ed. D. A. Bohlender, D. Durand, & P. Dowler (San Francisco, CA: ASP), 251

McLure, R. J., Kukula, M. J., Dunlop, J. S., et al. 1999, MNRAS, 308, 377

Mateos, S., Carrera, F. J., Alonso-Herrero, A., et al. 2015, MNRAS, 449, 1422

Mateos, S., Carrera, F. J., Barcons, X., et al. 2017, ApJL, 841, L18

Merloni, A., Bongiorno, A., Brusa, M., et al. 2014, MNRAS, 437, 3550

Namekata, D., & Umemura, M. 2016, MNRAS, 460, 980

Nenkova, M., Sirocky, M. M., Ivezić, Ž., & Elitzur, M. 2008a, ApJ, 685, 147

Nenkova, M., Sirocky, M. M., Nikutta, R., et al. 2008b, ApJ, 685, 160

Netzer, H. 2015, ARA&A, 53, 365

Noll, S., Burgarella, D., Giovannoli, E., et al. 2009, A&A, 507, 3

Myers, A. D., Palanque-Delabrouille, N., Prakash, A., et al. 2015, ApJS, 221, 27

Pâris, I., Petitjean, P., Aubourg, É, et al. 2012, A&A, 548, A66

Pâris, I., Petitjean, P., Aubourg, É, et al. 2018, A&A, 613, A51

Pitman K., Clayton G. C., Gordon K. D., 2000, PASP, 112, 537

Polletta, M., Tajer, M., Maraschi, L., et al. 2007, ApJ, 663, 81

Prevot, M. L., Lequeux, J., Maurice, E., Prevot, L., & Rocca-Volmerange, B. 1984, A&A, 132, 389

Rakshit, S., Stalin, C. S., & Kotilainen, J. 2020, ApJS, 249, 17

Ramos Almeida, C., Levenson, N. A., Alonso-Herrero, A., et al. 2011, ApJ, 731, 92

Ramos Almeida, C., & Ricci, C. 2017, NatAs, 1, 679

Rau, A., Kulkarni, S. R., Law, N. M., et al. 2009, PASP, 121, 1334

Rees, M. J., Silk, J. I., Werner, M. W., & Wickramasinghe, N. C. 1969, Nature, 223, 788

Ricci, C., Trakhtenbrot, B., Koss, M. J., et al. 2017, Nature, 549, 488

Ricci, C., Ueda, Y., Ichikawa, K., et al. 2014, A&A, 567, A142

Roseboom, I. G., Lawrence, A., Elvis, M., et al. 2013, MNRAS, 429, 1494

Runnoe, J. C., Brotherton, M. S., & Shang, Z. 2012, MNRAS, 422, 478

Salvato, M., Hasinger, G., Ilbert, O., et al. 2009, ApJ, 690, 1250

Schartmann, M., Meisenheimer, K., Camenzind, M., et al. 2005, A&A, 437, 861

Schartmann, M., Wada, K., Prieto, M. A., Burkert, A., & Tristram, K. R. W. 2014, MNRAS, 445, 3878

Schawinski, K., Urry, C. M., Virani, S., et al. 2010, ApJ, 711, 284

Schlafly, E. F., & Finkbeiner, D. P. 2011, ApJ, 737, 103

Schneider, D. P., Richards, G. T., Hall, P. B., et al. 2010, AJ, 139, 2360

Schwarz, G. 1978, The Annals of Statistics, 6, 461

Shen, Y., Richards, G. T., Strauss, M. A., et al. 2011, ApJS, 194, 45

Siebenmorgen, R., Heymann, F., & Efstathiou, A. 2015, A&A, 583, A120

Silva, L., Granato, G. L., Bressan, A., & Danese, L. 1998, AJ, 509, 103

Simpson, C. 2005, MNRAS, 360, 565

Skrutskie, M. F., Cutri, R. M., Stiening, R., et al. 2006, AJ, 131, 1163

Stalevski, M., Fritz, J., Baes, M., Nakos, T., & Popović, L. Č. 2012, MNRAS, 420, 2756

Stalevski M., Ricci C., Ueda Y., et al. 2016, MNRAS, 458, 2288

Stalevski M., Tristram K. R. W., Asmus D., 2019, MNRAS, 484, 3334

Stanley, F., Harrison, C. M., Alexander, D. M., et al. 2015, MNRAS, 453, 591

Suganuma, M., Yoshii, Y., Kobayashi, Y., et al. 2006, ApJ, 639, 46

Taylor, M. B. 2006, in ASP Conf. Ser. 351, Astronomical Data Analysis Software and Systems XV, ed. C. Gabriel et al. (San Francisco, CA: ASP), 666

Tanimoto, A., Ueda, Y., Odaka, H., et al. 2019, ApJ, 877, 95

Toba, Y., Oyabu, S., Matsuhara, H., et al. 2012, Publ. Korean Astron. Soc., 27, 335

Toba, Y., Oyabu, S., Matsuhara, H., et al. 2013, PASJ, 65, 113

Toba, Y., Oyabu, S., Matsuhara, H., et al. 2014, ApJ, 788, 45

Toba, Y., Oyabu, S., Matsuhara, H., et al. 2017, Publ. Korean Astron. Soc., 32, 93

Toba, Y., Ueda, Y., Matsuoka, K., et al. 2019a, MNRAS, 484, 196

Toba, Y., Yamashita, T., Nagao, T., et al. 2019b, ApJS, 243, 15

Toba, Y., Yamada, S., Ueda, Y., et al. 2020a, ApJ, 888, 8

Toba, Y., Wang, W.-H., Nagao, T., et al. 2020b, ApJ, 889, 76

Toba, Y., Goto, T., Oi, N., et al. 2020c, ApJ, 899, 35

Tristram, K. R. W., Burtscher, L., Jaffe, W., et al. 2014, A&A, 563, A82

Tristram, K. R. W., Meisenheimer, K., Jaffe, W., et al. 2007, A&A, 474, 837

Ueda, Y., Akiyama, M., Hasinger, G., Miyaji, T., & Watson, M. G. 2014, ApJ, 786, 104

Ueda, Y., Akiyama, M., Ohta, K., & Miyaji, T. 2003, ApJ, 598, 886

Ueda, Y., Eguchi, S., Terashima, Y., et al. 2007, ApJL, 664, L79

Urry, C. M., & Padovani, P. 1995, PASP, 107, 803

Véron-Cetty, M.-P., Joly M., Véron P., 2004, A&A, 417, 515

Vestergaard, M., & Peterson, B. M. 2006, ApJ, 641, 689

Vestergaard, M., & Wilkes B. J., 2001, ApJS, 134, 1

Vito, F., Brandt, W. N., Yang, G., et al. 2018, MNRAS, 473, 2378

Wada, K. 2012, ApJ, 758, 66

Wada, K. 2015, ApJ, 812, 82

Wada, K., & Norman, C. A. 2002, ApJL, 566, L21

Wada, K., Schartmann, M., & Meijerink, R. 2016, ApJL, 828, L19

Wang, J.-G., Dong, X.-B., Wang, T.-G., et al. 2009, ApJ, 707, 1334

Wright, E. L., Eisenhardt, P. R. M., Mainzer, A. K., et al. 2010, AJ, 140, 1868

Yang, G., Boquien, M., Buat, V., et al. 2020, MNRAS, 491, 740

York, D. G., Adelman, J., Anderson, J. E., Jr., et al. 2000, AJ, 120, 1579

Zamfir, S., Sulentic, J. W., Marziani, P., & Dultzin, D. 2010, MNRAS, 403, 1759

Zhuang, M.-Y., Ho, L. C., & Shangguan, J. 2018, ApJ, 862, 118